



Research article

Correlation of microstructure, texture, and mechanical properties of friction stir welded Joints of AA7075-T6 plates using a flat tool pin profile

Rahul Kesharwani^{a,b,*}, Kishor Kumar Jha^a, Murshid Imam^a, Chiranjit Sarkar^a,
Imad Barsoum^{b,c,**}

^a Department of Mechanical Engineering, Indian Institute of Technology Patna, Bihar, India, 801106

^b Department of Mechanical Engineering, Khalifa University, P.O. Box 127788, Abu Dhabi, United Arab Emirates

^c Department of Engineering Mechanics, Royal Institute of Technology – KTH, Teknikringen 8, Stockholm, 100 44, Sweden

ARTICLE INFO

Keywords:

Friction stir welding
Flat tool pin
Elastic modulus
Microstructural
Texture analysis
Microhardness

ABSTRACT

This study investigates the influence of square and hexagon tool pin profiles on the butt joint of AA7075-T6 plates through friction stir welding. In contrast to the AA7075-T6 base metal with a grain size of 32.736 μm , both square (4.43 μm) and hexagon (5.79 μm) pin profiles led to a significant reduction in grain size within the stir zone (SZ) of the weld cross-section. The SZ region exhibited a gradient in recrystallization and a notable fraction of high angle grain boundaries, attributed to continuous dynamic recrystallization influenced by variations in temperature and strain rate. Pole figure analysis revealed predominant shear texture elements (B/ \bar{B} and C) with minor A_1^*/A_2^* and A/\bar{A} , indicating elevated strains within the SZ. Orientation distribution function (ODF) analysis identified recrystallization texture elements such as Goss {110} <001>, cube {001} <101>, and P {011} <112>, along with shear texture components F {111} <112> and rotating cube (H) {001} <110>. Tensile and nanoindentation analyses demonstrated that the weld joint using a square-shaped pin profile exhibited higher strength, elongation, and elastic modulus compared to other weld joints. These findings suggest that the square tool pin geometry enhances material flow and grain refinement during welding, thereby improving the mechanical properties of the joint.

1. Introduction

The application of light materials to replace traditional heavy-weight materials to lower the fuel consumption capacity of vehicles and many other application fields, is the main emphasis of today's research. Aluminium materials come to mind immediately when considering uses for weight reduction application. Aluminium is, however, challenging to weld using traditional joining techniques (fusion welding) [1–3]. When welding aluminium alloys (AA) employing fusion process, various researchers discovered flaws as porosity, slag inclusion, excessive residual stress, voids, and solidification cracks [1–3]. Owing to the difficulties encountered in achieving fusion welds with elevated strength and robust resistance to fatigue and corrosion in the 7000 series of aluminium alloys,

* Corresponding author. Department of Mechanical Engineering, Indian Institute of Technology Patna, Bihar, 801106, India.

** Corresponding author. Department of Mechanical Engineering, Khalifa University, P.O. Box 127788, Abu Dhabi, United Arab Emirates.

E-mail addresses: rahul_1821me07@iitp.ac.in (R. Kesharwani), imad.barsoum@ku.ac.ae (I. Barsoum).

<https://doi.org/10.1016/j.heliyon.2024.e25449>

Received 19 September 2023; Received in revised form 20 January 2024; Accepted 26 January 2024

Available online 29 January 2024

2405-8440/© 2024 The Authors. Published by Elsevier Ltd. This is an open access article under the CC BY-NC-ND license (<http://creativecommons.org/licenses/by-nc-nd/4.0/>).

commonly employed in the aerospace, defense, automobile, railway, construction, and shipbuilding sectors [1,4–6], the application of fusion welding has been limited within advanced industries. These alloys are typically thought to be challenging to weld. The study of welding techniques for these alloys is crucial due to their widespread use in a variety of industries. Weight reduction is an important design factor in the aircraft industry, and aluminium, with its lower density than steel alloys, is a key element in this area [7,8]. Hence, to address the challenge of joining AA materials, friction stir welding (FSW) serves as a solid-state joining technique [9,10]. This joining technique finds its primary application in industries such as aerospace, defense, and automotive. This process was first invented in December 1991 when Wayne Thomas and his colleagues at The Welding Institute (TWI) in Cambridge, UK, developed the FSW method for joining aluminium alloys [8,11,12]. This FSW method has minimized the defects occurred by the conventional fusion welding of aluminium alloys and improved the joint quality and weld strength. Also, joining in this method is eco-friendly, safe, and non-hazardous, like TIG, MIG, and GTAW fusion welding methods [13,14].

Additionally, the FSW process is also applied to join various other materials, such as copper [15], magnesium [16], as well as high-strength materials like steel, Inconel, nickel, and titanium, among others [17–21]. More recently, the FSW process has been utilized for the fabrication of composite materials through the incorporation of reinforcing particles into an aluminium matrix (Al-matrix) [22,23]. This reinforcement has not only enhanced joint strength and hardness for diverse industrial applications but has also contributed to a reduction in the overall weight of the final composite product [8]. Additionally, the efficient joining of various aluminium alloys is currently accomplished using the friction stir additive manufacturing (FSAM) technique, an advanced solid-state additive manufacturing (AM) approach [24]. The process of joining aluminium alloys in FSAM is similar to the FSW process. By utilizing FSAM methods, successful joints were produced through systematic layering of multi-layered structures on top of each other [24].

Moreover, currently the conventional friction stir welding is used in advance version of welding technique such as friction stir vibration welding (FSVW) for homogenous mixing of reinforcement particle into the aluminium matrix during welding [25,26]. During the FSVW process, the workpieces of aluminium alloy are vibrated perpendicular to the weld line, and simultaneously, reinforcement particles are integrated into the weld. This vibration results in a reduction of grain size in the weld region and enhances the uniform distribution of particles.

Nonetheless, despite the promising advantages offered by the FSW joining method, the design of FSW tools has continuously evolved to address the increasing demands and complexities associated with producing industry-compliant components, encompassing strict control over physical, mechanical, and dimensional attributes [27–29]. While intricate tool geometries have been suggested based on experimental trials [29–31], straightforward (simple) tool designs have been favoured due to their cost-effectiveness and ease of utilization. Several researchers have proposed tool geometries with intricate features, but selecting the appropriate FSW tool material and shape is a critical pre-experiment consideration, as these factors significantly influence weld quality [27,29]. Altering the tool's dimensions can lead to variations in mechanical properties. Therefore, the adoption of simpler tool designs might present a pragmatic approach in terms of cost-efficiency, provided they can still yield welds of high quality [29].

Moreover, FSW tools featuring multiple flats machined on a cylindrical surface have been recognized for their effectiveness in improving material mixing and attaining high-quality welds [32]. Four flats are considered to be the optimum number that can be machined off a cylindrical surface in this category [33]. Furthermore, researchers have noted that the pulsating stirring action and localized heat generation on the flat surface are more pronounced in comparison to the curved surface of the tool probe [34]. Elangovan et al. [35] determined how different tool pin profiles affected FSW joints. These pin profiles comprised square, triangular, threaded, tapered, and straight cylindrical pins. The experiment showed that the square pin profile produced better results than the other profiles. The basic tool pin design features like straight, tapered, threaded cylinders and some polygon tool pin designs (triangle, square, pentagon, and hexagon) are used for joining the workpiece by the FSW techniques [36]. Moreover, different shoulder surface design features like concave, convex, scrolled, and spiral were also integrated with the pin features for improving the material flow and getting the desired quality of joint [37,38]. The different tool pin designs and shapes change the microstructure and mechanical properties of the FSW joint.

Additionally, Ilango et al. [38] studied the effects of the three simple pin geometries (straight cylinder, tapered cylinder, and threaded cylinder) on the microstructure and mechanical properties of the FSW of dissimilar aluminium alloys (AA) 6061 and 5086 plates. The defect-free, higher mechanical properties, and excellent material mixing were reported by the threaded cylindrical tool pin profile. The homogenous distribution of precipitates, onion ring flow pattern, and fine grains were observed on the weld nugget zone when a threaded pin was used. Furthermore, Masoumi et al. [39] conducted a study exploring distinct tool pin geometries (conical pin, stepped conical pin, threaded cylindrical pin, and cubic pin), shoulder geometries (flat, raised spiral, and raised fan), as well as the effects of process parameters on material flow and mechanical properties in FSW of dissimilar aluminium alloys. Among the investigated configurations, the threaded cylinder, straight cylinder, and square tool pin profiles were associated with sound joint quality [39]. Additionally, the raised fan shoulder surface exhibited an improved capability to enhance material flow from the shoulder edge to the pin, promoting a smooth material flow across the raised fan shoulder surface.

Further, Li et al. [40] reported the material flow and temperature rise variation on the two different pin profiles, full threaded and half threaded, in friction stir spot welding (FSSW) of 2A12-T4 aluminium alloy. The findings indicated that the half-threaded pin design led to a broader bonding width in comparison to the full-threaded pin profile. Also, the peak temperature rises in half-threaded pins were lower than those in full-threaded pins during welding. Mastanaiah et al. [41] reported the effect of the hybrid tool pin (conical thread with triangular pin features) profile in the FSW of AA2219-T6. In the weld nugget zone, the coarser grains were reported at the shoulder region, whereas at the bottom zone, the finer grains were observed for both hybrid and conventional tool pin profiles. The weld quality made by the threaded tool pin was inferior to that of the hybrid tool. Moreover, the bobbin tool pin features used for FSW of aluminium alloy plates were also reported by several researchers [42,43].

The objective of this study is to investigate the evolution of microstructure and texture in the stir zone (SZ) region of joints formed using square (SQ) and hexagon (HX) shape tool pin profiles. A comprehensive experimental analysis was conducted to assess the impact of a flat tool pin profile, comprising both square and hexagon shapes, on the friction stir welding of AA7075-T6. Despite the thorough experimental analysis, the interplay between strength, microstructure, and texture, particularly at the joint interface when employing square and hexagon-shaped tool pins to join AA7075-T6 plates, has not been extensively explored. This research establishes a correlation between strength, microstructure, texture, nanoindentation behaviour, and microhardness, providing valuable insights into the properties of the weld joint and the influence of tool pin profiles. Optical microscopy (OM), field emission scanning electron microscopy (FESEM), electron backscattered diffraction (EBSD), nanoindentation, microhardness, and tensile tests were conducted to determine the microstructural and mechanical properties of the weld joint, and the results were compared for both square and hexagon-shaped tool pin profiles.

2. Material and methods

The selected material for the present study is aluminium alloy plates of the 7075-T6 grade. Two of these AA7075-T6 plates are utilized for the butt joint configuration through FSW experiments. Fig. 1(a) illustrates the diagrammatic representation of the FSW plates along with the tools. The size of each plate is 100 mm, 50 mm, and 5 mm in length, width, and thickness, respectively (see Fig. 1(c)). The chemical composition of the AA7075-T6 plate is given in Table 1. For the experiment, a 5-T capacity FSW machine (M/S RV Machine Tools, Coimbatore, India) is used. Significant clamping is crucial within the FSW machine bed to enable the clamps to withstand the forces (axial and lateral) exerted during the welding process. This ensures that the plates remain stable and aligned without bending or misalignment.

Moreover, a crucial element in the FSW process for joining the two plates is the FSW tool. In present study, two distinct tool pin profiles, namely square (SQ) and hexagon (HX) shapes, are employed for weld joining. These tools are fabricated from H-13 steel material, and their chemical composition is detailed in Table 1. The specific dimensions of the tool pin profiles are illustrated in Fig. 1(b). The FSW tool maintains uniform specifications across both pin profiles, with a shoulder diameter of 25 mm, pin diameter of 7 mm,

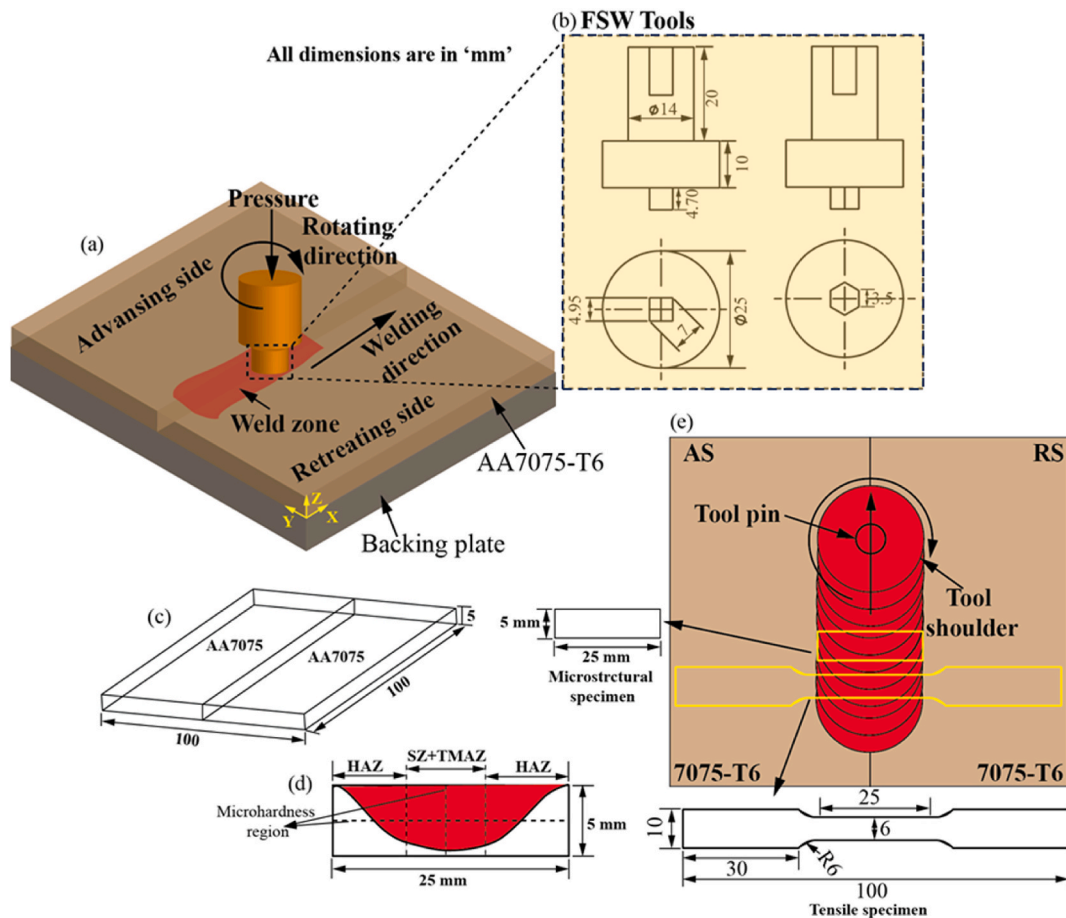


Fig. 1. Schematic representations of (a) the FSW tool position with workpiece AA7075-T6, (b) FSW tool with square and hexagon shaped pins, (c) dimensions of AA7075-T6 plate, (d) size of microhardness specimen, and (e) dimensions of tensile and microstructural samples, respectively.

Table 1
AA7075-T6 workpiece and H-13 steel tool material chemical composition [44,45].

AA7075-T6	Cr	Cu	Fe	Mg	Mn	Si	Ti	Zn	Al
	0.18	1.40	0.11	0.25	0.05	0.25	0.07	4.8	Balance
H-13 steel	C	Cr	Mn	Mo	Si	V	W	Ni	Fe
	0.51	5.5	0.413	1.52	1.26	1	0.02	0.19	Balance

and pin length of 4.7 mm. The square and hexagonal pin shapes are derived from the initial 7 mm-diameter cylindrical pin profile. The experimental process follows a sequence wherein the SQ-shaped pin profile is employed for the initial set of experiments, followed by the utilization of the HX-shaped pin profile for the subsequent set. The optimized process parameters for plate joining are determined as 850 rpm for rotational speed and 55 mm/min for welding speed [24,46]. Moreover, subsequent to the joining of the two plates, the evaluation of the joint was carried out through the extraction of a weld specimen from the region where the plates were joined. To achieve this, a wire-cut electric discharge machine (WEDM) was employed. Microstructure analysis and samples for tensile testing were acquired from the welded regions associated with both the SQ and HX pin profiles. This facilitated a comparative analysis of the impact on joint quality and material properties, considering variations in the pin profiles. Additionally, Fig. 1(e) depicts the schematic illustration indicating the placement for cutting the tensile specimens, along with the measurements of the weld samples.

Thereafter, the AA7075-T6 welded specimen cross-section region is polished for a clear picture of the microstructure zone. The weld specimen undergoes a polishing process using various grades (ranging from 200 μm to 3000 μm) of SiC emery paper. This procedure effectively eliminates dirt particles and oxide layers from the weld cross-section, yielding a refined and clean surface.

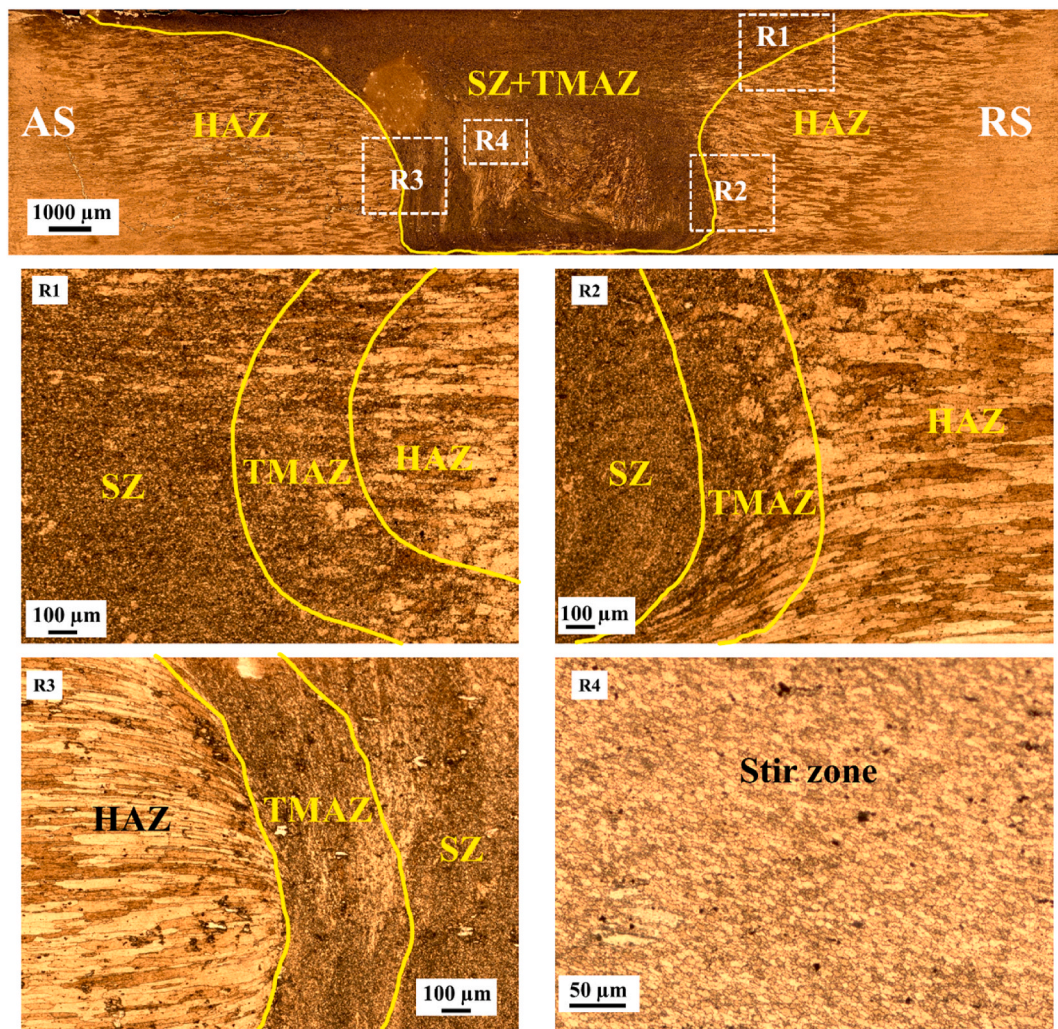


Fig. 2. Optical macrograph image of weld cross-section using square shape FSW pin.

Subsequently, the polished sample is carefully rubbed to achieve a mirror-like finish through the use of diamond paste with particle sizes of 3 μm , 1 μm , and 0.25 μm . Following the polishing steps, the mirror-finished sample is subjected to etching using Keller's reagent, comprising 1.5 ml of HCl, 2.5 ml of HNO_3 , 1 ml of HF, and 95 ml of distilled water. For obtaining the optical macrograph images of the weld cross-section and its different regions, an optical microscope (Zeiss, Axio Imager, M2m) is utilized. This approach enables the acquisition of clear and detailed images of the sample's structure.

Additionally, a field emission scanning electron microscope (FESEM) machine (Zeiss, GEMINI 500) is used to examine the weld cross-section's surface in the central stir zone region using an electron backscattered diffraction (EBSD) analysis. Subsequently, mechanical testing of the weld specimen is carried out through microhardness and tensile tests. In the case of the microhardness test, the central area of the weld cross-section (as illustrated in Fig. 1(d)) undergoes examination with a Vickers microhardness testing machine (Zwick Roell). This test is executed with an indenter load of 100 gf and a dwell time of 10 s, with a spacing of 500 μm between successive indenter locations. Then, the tensile test is performed on a universal testing machine (UTM) (Zwick Roell) with a capacity of 50 kN, utilizing a strain rate of 0.001 1/s. The design of the tensile specimen is selected from the ASTM E08 standard. After the tensile test of the specimen, fracture surface images were taken from the FESEM machine. Further, the mechanical properties of weld SZ, TMAZ, and HAZ at room temperature (23 $^{\circ}\text{C}$) are evaluated by using a nano-indentation machine. A nano-indentation test was performed on the Bruker Hysitron Nano-indenter T1 950 machine (Bruker Nano Inc., USA). A pyramidal-shaped tip of radius ~ 100 nm made of diamond material is used for indentation. Nanoindentation is a rapid measurement method that provides mechanical property data, including modulus and hardness. For this nano-indentation testing, samples were prepared following the standard metallographic sample preparation procedure, which involved common mechanical polishing on SiC emery papers and subsequent polishing on diamond pastes until reaching a size of approximately 0.1 μm . Each indentation during testing was performed with a maximum load of 50 mN and a dwell time of 2 s.

3. Results and discussion

3.1. Macrostructural analysis

Fig. 2 shows an optical macrograph (OM) image of the AA7075-T6 plate weld cross-section which formed using the SQ pin profile. In the current analysis, the single-pass FSW process is used, and defect-free, high-quality joints are obtained after welding. Several common defects encountered in FSW of aluminium alloys include kissing bond, void, tunnel, and crack [3,7,8]. These defects are often attributed to improper material mixing, excessive heat generation, unsuitable tool selection, and suboptimal process parameter choices. However, it is worth noting that the utilization of the SQ-shaped pin profile has led to the achievement of sound joints with uniform material mixing, leading to improved joint quality. The FSW tool pin is compressed downward between the two AA7075-T6 plates at the interface region of the butt joint configuration position, while the shoulder is pushed against the surfaces of the materials being welded [47]. The workpiece material experiences significant plastic deformation as a result of the tool's frictional heat generation with the plates during a combination of rotational and translational motion. Due to the presence of flat faces on the FSW pin, a pulsating stirring action is observed at the tool pin/workpiece contact region [48,49]. This leads to more deformation and thermal softening of the material during welding. Also, the optimized number of flat faces present on the tool pin periphery is reported by Kesharwani et al. [49]. They found that the SQ shape pin profile gives better mixing compared to other polygon pin profiles (hexagon and pentagon) during FSW of aluminium alloy.

Furthermore, various areas (R1 to R4) are marked in the weld cross-section OM image of the FSWed joint used with the SQ-shaped pin. R3 and R2 regions are marked on the advancing side (AS) and retreating side (RS) at the interface of the SZ, heat affected zone (HAZ), and thermo-mechanically affected zone (TMAZ) regions, respectively. During the FSW process, three different weld zones, such as SZ, HAZ, and TMAZ, are formed based on grain size. These different weld regions are formed because of differences in heat generation and temperature rise (thermal softening) inside the materials. The transition zone between the SZ and HAZ regions is called the TMAZ in the FSW/processing [50]. This zone experiences a lower peak temperature and strain rate than SZ. It has been observed that this zone undergoes partial dynamic recrystallization. The HAZ exists after the TMAZ region. This zone only experiences the thermal cycle. According to Mahoney et al. [51], the temperature rise in the HAZ during welding of the heat-treatable aluminium alloy material is around 250 $^{\circ}\text{C}$. At this temperature, the grain structure in the HAZ region was the same as the parent material. However, the dissolution or coarsening of the precipitates is observed in this region. Here in R2 and R3, the different grain sizes show elongated and fine and ultra-fine grains at the HAZ, TMAZ, and SZ regions due to different temperature rises and plastic deformations during welding. Similarly, the R1 region just below the shoulder surface region shows the differences in grain size in the SZ, HAZ, and TMAZ regions.

Furthermore, the R4 region is marked at the weld stir zone. Here, the ultra-fine grain refinement was observed after welding with an SQ-shaped FSW tool pin. The weld SZ region develops a recrystallized, fine-grained microstructure due to friction heating and plastic deformation. This region experiences the highest peak temperature and strain rate. The SZ region is also known by different names, such as nugget zone (NZ), weld nugget zone (WNZ), or dynamic recrystallized zone (DRX) [50]. This region observed the onion-ring pattern of plastically deformed material flow. The dimension and shape of the SZ region depend on the process parameter, tool design, heat generation rate, and thermal conductivity of the material used in the FSW process [51].

The temperature and strain rate in the FSW are influenced by various variables, including tool rotation speed, traverse speed, and tool shoulder diameter [8,51]. Despite the linear relationship between tool rotational speed, traverse speed, and shoulder diameter, the temperature in the weld zone increases with higher tool rotational speed but decreases with an increase in traverse speed. Moreover, an enlarged shoulder diameter not only improves the tool's heat-carrying capacity but also increases frictional heat. An escalation in traverse speed elevates the strain rate and reduces the temperature in the weld zone, leading to the formation of a fine grain structure

[52,53]. Following intense plastic deformation and exposure to elevated temperatures, the weld zone may undergo dynamic recovery and dynamic recrystallization. This process results in a highly refined grain structure within the weld zone region and accordingly dimension and shape of stir zone changes [51,52–54]. The defect-free, good material mixing, and ultra-fine grain refined in the SQ-shaped FSW tool pin result in improvements in the tensile strength and mechanical properties of the joint, which will be further discussed in the tensile stress-strain analysis of the weld specimen.

Furthermore, the weld cross-section OM image obtained from the hexagon shape pin profile is shown in Fig. 3. Here, defects are observed at the AA7075-T6 plate bottom region towards the RS of the FSW tool. These defects arise as a result of inadequate material flow at the lower region of the plate. Additionally, Patel et al. [33] noted a defect within the weld cross-section when employing the HX-shaped pin profile. However, Kesharwani et al. [49] stated that the extra torque generated by the presence of a flat pin during FSW is less pronounced in the case of an HX-shaped pin profile as compared to an SQ-shaped pin profile. A higher torque value during the FSW process results in a high fraction of material thermal softening during welding, as reported by Andrade et al. [55]. Also, the workpiece/tool contact length is shorter in the HX pin profile compared to the SQ-shaped pin profile [49]. Due to this, the heat generation and thermal softening of the AA7075-T6 are low during welding in the case of the HX-shaped pin profile, and as a result, the defect at the bottom region is observed.

Further, different regions R1 to R4 (see Fig. 3) are marked in the weld cross-section OM image. Grain size variation on SZ, TMAZ, and HAZ is clearly seen in the R1 region. The grains in the TMAZ region exhibit a finer size, while those in the HAZ region appear coarser. Moreover, R2 and R3 are marked at the SZ region, where ultra-fine grain size is observed. Due to the very high temperature, high strain rate, and severe plastic deformation in the SZ region, the ultra-fine grains are observed [56,57]. Further, R4 is marked at the bottom location of the plate, here the tunnel and void defects are clearly visible. The defects in the HX-shaped pin profile FSW joint are formed due to the loss of material or mass imbalances during material flow around the tool pin. Also, Chitturi et al. [58] reported that

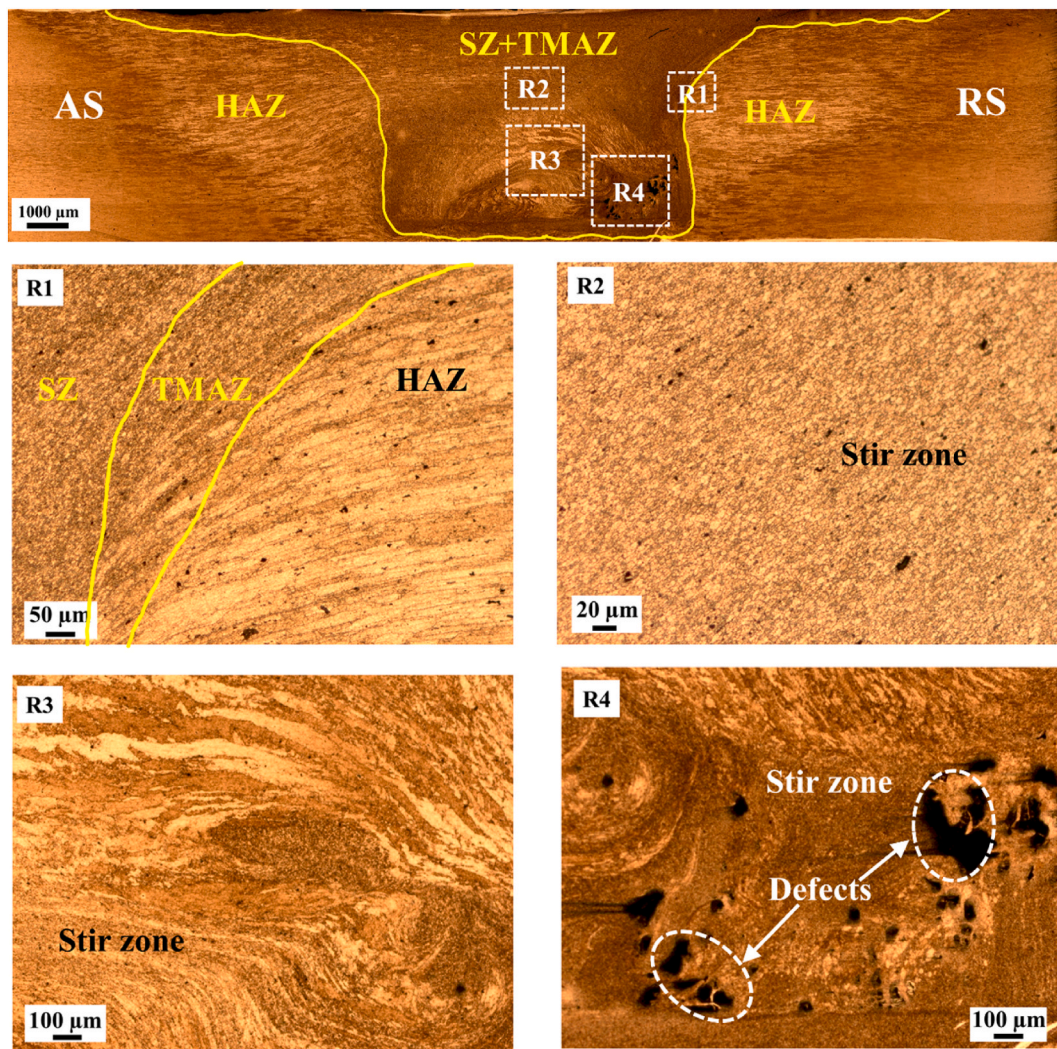


Fig. 3. Optical macrograph image of weld cross-section using hexagon shape FSW pin.

tunnel defects are usually found in the bottom portion of the processed region. The inappropriate selection of the welding parameter and tool design is responsible for the tunnel defect on the welded surface [59,60]. The optimized process parameter is used to join the AA7075-T6 plate, and the process parameter is the same for both cases. Therefore, in the present case, tool shape is the main deciding parameter for the formation of defects in the FSW process.

3.2. Microstructural and crystallographic texture analysis

Moreover, the EBSD analysis is utilized to evaluate the microstructural characteristics of AA7075-T6 base metal (BM) and FSWed joint using by SQ, and HX shape pin profiles. The base metal (AA7075-T6) inverse pole figures (IPFs) map, which reveals the crystallographic orientation of the grains, is shown in Fig. 4(a). The IPF map shows that the 7075-T6 BM contains coarser, elongated grains that are parallel to the rolling direction (RD). Fig. 4(b) show the base metal low-angle grain boundaries (2° - 15°) and high-angle grain boundaries (15° - 65°) fraction. Fig. 4(c) shows the grain size distribution, with an average grain size of $32.736 \mu\text{m}$. Additionally, Fig. 4(d) shows a misorientation angle distribution map for the BM, providing details on the distribution of misorientation angles inside the grains.

Furthermore, Fig. 5(a) illustrates the IPF map obtained from EBSD analysis, representing the crystallographic orientation of grains in the middle region of the AA7075-T6 FSWed plates using an SQ shape pin. Notably, the IPF map shows that the middle stir zone of the Al-matrix contains an ultra-fine grain structure. The fractions of high-angle grain boundaries (f_{HAGB}) and low-angle grain boundaries (f_{LAGB}) in the SQ shape pin FSWed joint are shown in the grain boundary plot in Fig. 5(b). The analysis indicates a notable occurrence of high-angle grain boundaries, constituting a fraction of 0.864, while low-angle grain boundaries are relatively less prevalent, comprising a fraction of 0.136. To accurately characterize the microstructure and grain boundaries in FSW of aluminium alloys the misorientation angles within the 0° - 2° range is commonly excluded [61,62]. By doing so, we can focus on the significant grain boundaries and avoid misinterpreting small-angle misorientations that may result from dynamic recrystallization or the presence of the nugget region. Therefore, we neglect the 0° - 2° misorientation angle fraction presence in the EBSD scan region. Instead, we consider the range of 2° - 65° as fraction 1, and subsequently, we illustrate the fractions of LAGBs and HAGBs in the grain boundary distribution plot (see Fig. 5(b)).

High-angle grain boundaries denote regions where the misorientation between neighbouring grains exceeds a specific threshold,

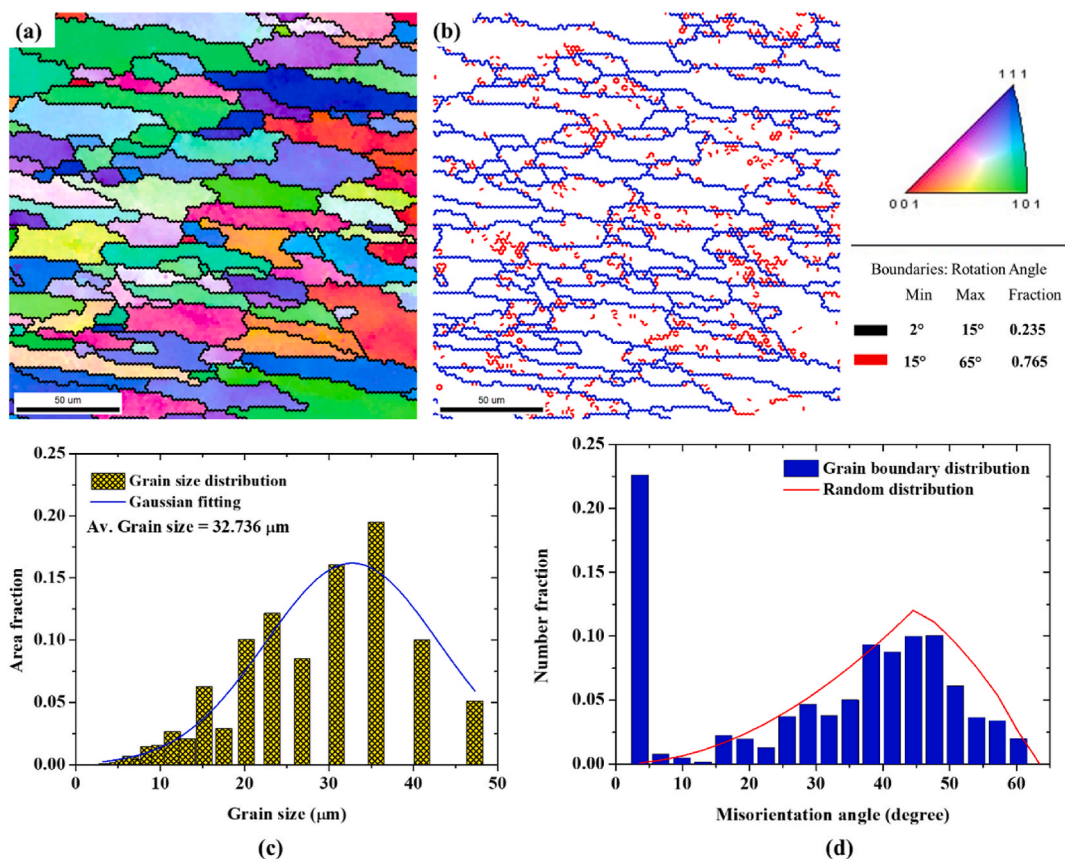


Fig. 4. Plate of AA7075-T6 base metal: (a) EBSD inverse pole figure map, (b) Grain boundary distribution emphasized for low angles (2° - 15°) and high angles (15° - 65°), (c) Chart illustrating the distribution of grain sizes, and (d) Graph depicting the distribution of misorientation angles.

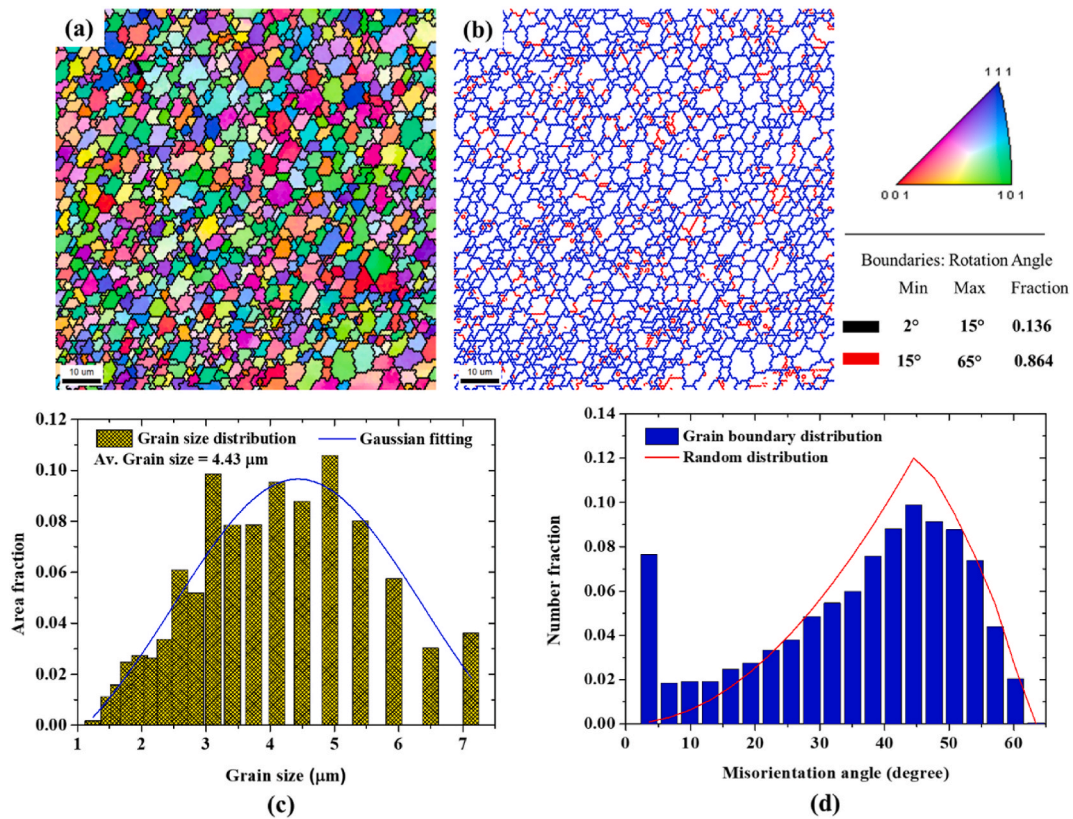


Fig. 5. SZ region of AA7075-T6 welded plate using square-shaped FSW pin: (a) EBSD inverse pole figure map, (b) Grain boundary distribution emphasized for low angles (2°-15°) and high angles (15°-65°), (c) Chart illustrating the distribution of grain sizes, and (d) Graph depicting the distribution of misorientation angles.

while low-angle grain boundaries represent smaller misorientations. The friction stir welding process with an SQ-shaped pin leads to pronounced temperature elevations in its vicinity. Consequently, multiple restoration mechanisms come into play concurrently, including continuous dynamic recrystallization (CDRX), discontinuous dynamic recrystallization (DDRX), and dynamic recovery (DRV). Dislocations inside grains are destroyed and rearranged during DRV, which lowers the amount of stored energy [61]. CDRX is a term used to describe the development of new grains within parent grains, which helps refine grains. Contrarily, DDRX involves the nucleation and development of new grains in high-strain areas [62]. When using a SQ-shaped pin during the FSW process, these restorative mechanisms together affect the microstructure and properties of the welded joint. The stir zone region develops a recrystallized fine-grained microstructure due to friction heating and plastic deformation. This region experiences the highest peak temperature and strain rate. The low dislocation density inside the recrystallized grain was reported by some researchers [50,63]. However, the other researcher found a high density of sub-grains [64], dislocation [65], and sub-boundaries [66] in the recrystallized grain of the nugget zone. The process involves intense plastic deformation and dynamic recrystallization, both contributing to the development of fine-grained structures that subsequently enhance the material's strength and hardness.

Furthermore, Moradi et al. [67] observed the occurrence of static recrystallization (SRX) during the cooling phase subsequent to the FSW process. High stacking fault energy (SFE) aluminium alloys undergo rapid dynamic recovery, causing dislocation buildup and annihilation [68]. However, during the FSW process, dislocations align to generate sub-grain boundaries with 2° to 5° grain misorientations. Dislocations reorganize inside sub-grain boundaries, forming low-angle grain barriers (LAGBs) with 5° to 15° misorientations. LAGBs become less stable and become more stable high-angle grain boundaries (HAGBs) with misorientations beyond 15° as CDRX dominates during FSW. FSW restoration in aluminium alloys begins with DRV and then CDRX [57–59].

The use of the SQ-shaped pin in the weld's AA7075-T6 stir zone results in a noticeable improvement in joint strength, as evidenced by an increased proportion of HAGBs (0.864). Moreover, this region exhibits significant grain refinement. The existence of second-phase particles during the FSW process initiates the mechanism of particle-stimulated nucleation (PSN). These particles hinder grain growth in the weld zone [68,69]. The IPF map illustrates that the formation of precipitates during FSW of AA7075-T6 material effectively restricts grain expansion, resulting in the development of ultra-fine grain sizes. Consequently, the PSN and CDRX mechanisms play crucial roles during the FSW process, enabling the achievement of ultra-fine grain refinement in the weld zone when employing an SQ-shaped pin profile.

Fig. 5(c), illustrate the distribution of grain sizes within the weld SZ region fabricated by using an SQ shape pin profile. Grain size

distribution plot revealed the 4.43 μm is the estimated average grain size within the SZ. This finding suggests effective blending at the interface of the two AA7075-T6 plates during welding, which leads to a consistent dispersion of grain sizes. The curve that depicts the frequency of various types of grain boundaries in the SZ region is shown in Fig. 5(d). Notably, the grain boundary distribution curve closely resembles the random misorientation curve. According to this alignment, the grain boundaries in the welded region adhere to a pattern of random misorientation, which is anticipated that a well-homogenized mixing AA7075-T6 material at the weld zone. Moreover, a study by Salih et al. [70] reported that a higher proportion of HAGBs in the SZ area contributes to an improved tensile performance of the weld specimen. Grain boundaries that have misorientation angles that are greater than a certain threshold is known as HAGBs. In the welded area, the presence of HAGBs can improve mechanical properties, such as improved strength and toughness. Overall, our findings show that a higher proportion of HAGBs has a positive impact on the tensile performance of AA7075-T6 welded plates with a SQ-shaped FSW tool pin.

Fig. 6(a) displays the IPF map obtained through EBSD analysis, represent the crystallographic orientation of AA7075-T6 FSW joints fabricated with the HX-shaped pin profile. The IPF provides information about the crystallographic orientation of the material's grains. The results indicated a remarkable refinement in grain size in the FSWed joint made using the HX shape pin profile. This indicates that the grains within the material were notably reduced in size compared to those present in the AA7075-T6 base metal. Moreover, it was found that the SQ shape pin generates more heat during the FSW process compared to the HX shape pin profile due to the larger contact area between the pin and workpiece [49]. This increased heat generation leads to greater thermal softening of the material, resulting in the formation of stronger high-angle grain boundaries when compared to the utilization of the HX-shaped pin. Additionally, the larger material flow and mixing during welding with the SQ shape pin promotes the formation of an increased fraction of HAGBs. Conversely, the insufficient temperature rises and thermal softening in the case of the HX shape pin during welding lead to the formation of a lower fraction of HAGBs. Instead, the investigation showed that the HX shape pin profile AA7075-T6 plate weld zone had a larger quantity of LAGBs.

Fig. 6(b) depicts the distribution plot of HAGBs and LAGBs. The analysis indicated that the f_{LAGBs} is 0.388, while the f_{HAGBs} is 0.612 in the FSWed AA7075-T6 material when using the HX shape pin profile. The presence of a lower fraction of HAGBs and a higher fraction of LAGBs in the FSWed joint using the HX shape pin profile compared to joint made by SQ shape pin profile is attributed to the low thermal softening of the material and insufficient material mixing. This results in a distinct grain boundary distribution compared to the SQ shape pin profile. In summary, the EBSD analysis indicated that the FSW joint obtained using the HX shape pin exhibited

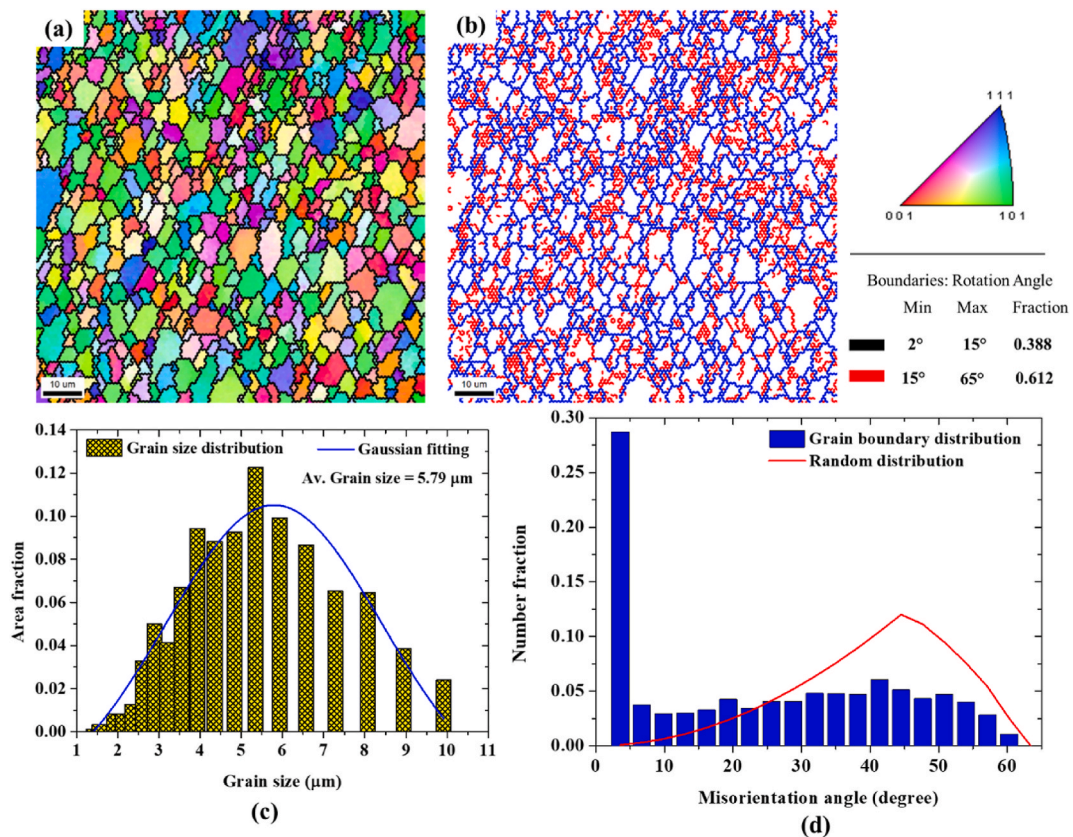


Fig. 6. SZ region of AA7075-T6 welded plate using hexagon-shaped FSW pin: (a) EBSD inverse pole figure map, (b) Grain boundary distribution emphasized for low angles (2°-15°) and high angles (15°-65°), (c) Chart illustrating the distribution of grain sizes, and (d) Graph depicting the distribution of misorientation angles.

ultra-fine grain refinement.

Fig. 6(c) depicts the plot showcasing the distribution of grain sizes within the welded SZ areas using the HX-shaped pin profile. The SZ middle region exhibits an average grain size of $5.79 \mu\text{m}$. It is to be observed that this value is higher than SQ shape pin weld zone grain size ($4.43 \mu\text{m}$) and lower than base material AA7075-T6 ($32.736 \mu\text{m}$). The use of the HX-shaped pin in the AA7075-T6 weld SZ results in improved grain refinement, which is attributed to the enhanced mixing of the AA7075-T6 material during the welding process. The presence of smaller grain sizes suggests the possibility of enhancing tensile loading characteristics, a topic that will be further explored in the subsequent section on tensile properties.

Fig. 6(d) illustrates the plot detailing the distribution of misorientation angles. It's evident that the curve representing misorientation angles in the HX-shaped weld SZ region doesn't precisely follow the pattern of a random distribution curve. It is noteworthy that between misorientation angles of 35° and 50° , the grain boundary distribution curve significantly deviates from the random distribution curve. On the other hand, the random distribution curve closely resembles the grain boundary distribution plot when looking at the misorientation plot for the SQ-shaped pin AA7075-T6 weld specimen (as shown in Fig. 5(d)). Overall, the EBSD study suggest that using a HX-shaped pin profile for welding results in the existence of finer grain sizes and a higher level of grain refinement than using the AA7075-T6 base metal. Furthermore, it is noteworthy that, within a particular range of misorientation angles, the distribution of misorientation angles in the FSW AA7075-T6 joint produced using the HX-shaped pin profile deviates from the pattern of a random distribution curve. On the other hand, when the SQ-shaped pin is employed for fabricating AA7075-T6 FSW joints, there is a more consistent alignment observed between the grain boundary distribution plot and random distribution curve.

Further, the grain orientation spread (GOS) map obtained from EBSD analysis of FSWed AA7075-T6 workpiece SZ region by using SQ and HX shape pin profile is shown in Fig. 7(a and b), respectively. GOS maps are used to differentiate between recrystallized and deformed grains by restricting the misorientation angle to less than 2° for recrystallized grains and considering the rest as deformed. A value of $\text{GOS} \leq 2^\circ$ is used as a criterion to identify recrystallized grains during the FSW process. The GOS map is valuable in distinguishing strain-free (recrystallized, $\leq 2^\circ$ shown in blue) and deformed grains ($>2^\circ$ shown in green) in the SZ region of the FSW joint. The fraction of recrystallized grains is higher in the AA7075-T6 weld made using an SQ-shaped pin profile (as shown in Fig. 7(a)) due to severe plastic deformation, strain rate, and thermal softening during the FSW process. The deformation of the AA7075-T6 material at high temperature results in an increased volume fraction of recrystallized grains when using the SQ-shaped pin profile compared to the HX-shaped pin profile. According to the GOS map, approximately 95 % of the grains were recrystallized in the AA7075-T6 weld region using the SQ-shaped pin profile, while in the case of the HX-shaped pin profile, approximately 85 % of the grains are recrystallized. Additionally, Table 2 presents a comparison of the average grain size, fraction of low and high angle grain boundaries, and fraction of recrystallized grain in the SZ region of the AA7075-T6 weld joint fabricated using SQ and HX shape tool pin profiles.

The texture retained within a material after undergoing mechanical processes like FSW holds a significant influence over material

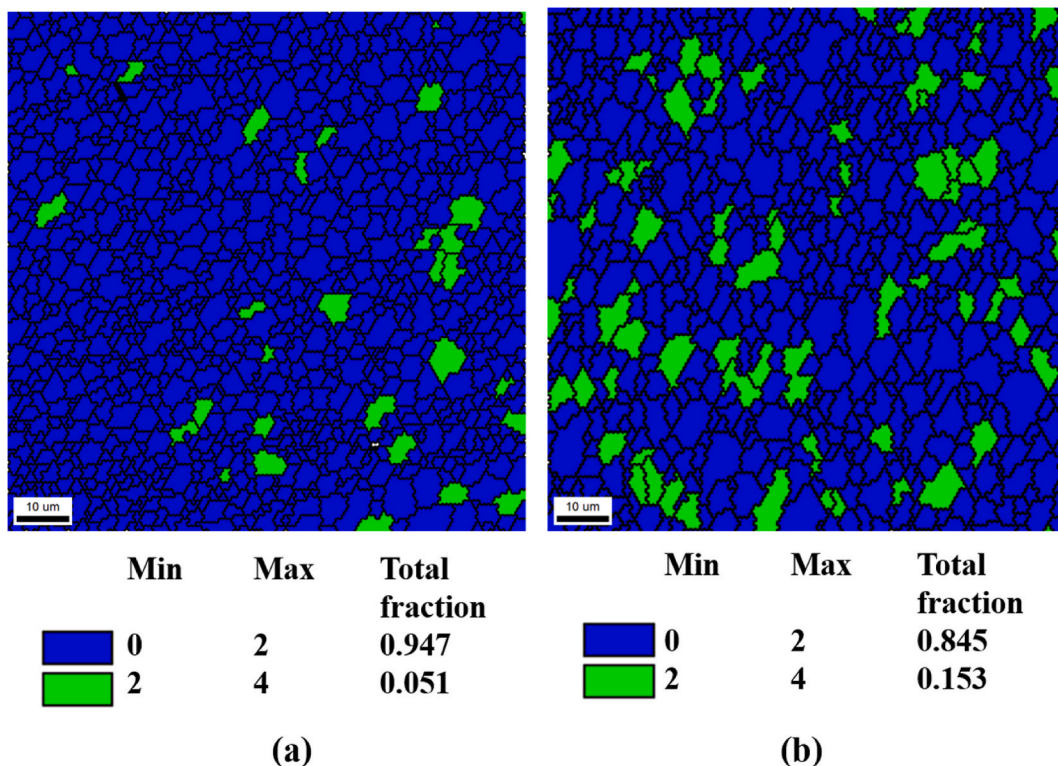


Fig. 7. GOS maps of AA7075-T6 plate welds using (a) square-shaped, and (b) hexagon-shaped, pin profiles.

Table 2

Grain size, fraction of high and low angle grain boundaries, and recrystallized grain in the SZ region of the AA7075-T6 FSW joint.

AA 7075-T6 FSW joint at SZ	Average grain size	High angle grain boundaries fraction	Low angle grain boundaries fraction	Fraction of recrystallized grain
Square pin	4.43 μm	0.864	0.136	0.947
Hexagon pin	5.79 μm	0.612	0.388	0.845

strengthening mechanisms. For metals with a face-centered cubic (FCC) structure, the primary textures following FSW typically relate to simple shear deformation. Pole figures (PFs) and orientation distribution functions (ODF) are frequently used by researchers to observe and evaluate these textures within the SZ of an aluminum alloy. Fig. 8(a and b) show the proposed elements of basic shear texture superimposed onto (001), (101), and (111) pole figures, each of corresponding to a different crystallographic orientation, in the context of FCC materials [71,72]. Moreover, ideal texture components superimposed on ODF parts at various angles, such as $\varphi_2 = 0^\circ, 45^\circ,$ and $65^\circ,$ are presented (see Fig. 8(a and b)). These theoretical components for FCC materials are also superimposed with the observed PF and ODF sections to reveal the material’s current texturing. By comparing the proposed elements with the observed texture, the types and orientations of textures induced within the material by the FSW process can be determined. This analysis furnishes valuable insights into the changes in microstructure and mechanical properties of post-welding/processing. Fig. 9(a and b) illustrate the PF and ODF plots acquired from EBSD analysis of the base metal AA7075-T6. The PFs for the (001), (101), and (111) crystallographic planes within the BM depict a random distribution of texture components (see Fig. 9(a)). The grain structure in the base material remains unchanged, attributed to insufficient heat generation and plastic deformation to induce significant modifications.

Fig. 10 (a and b) depicts the pole figure and orientation distribution function map for friction stir-welded joints of 7075-T6, employing an SQ-shaped pin profile. The dominant shear texture elements B/ \bar{B} and C are consistently evident across all regions, indicating pronounced shear deformation. Additionally, small amounts of the lower strain $A_1^*, A_2^*,$ and A/\bar{A} shear elements can be found. In the ODF map, analysis is conducted at various angles ($\varphi_2 = 0^\circ, 45^\circ,$ and 65°) and compared with theoretical components. This examination of ODF map unveils the existence of recrystallization texture elements, including P {011} $\langle 112 \rangle,$ Goss {110} $\langle 001 \rangle,$ and cube {001} $\langle 101 \rangle,$ as well as shear texture components like rotating cube (H) {001} $\langle 110 \rangle,$ and F {111} $\langle 112 \rangle.$ Together with the dominance of the primary shear texture components (B// \bar{B} and C) and the existence of these recrystallization texture elements

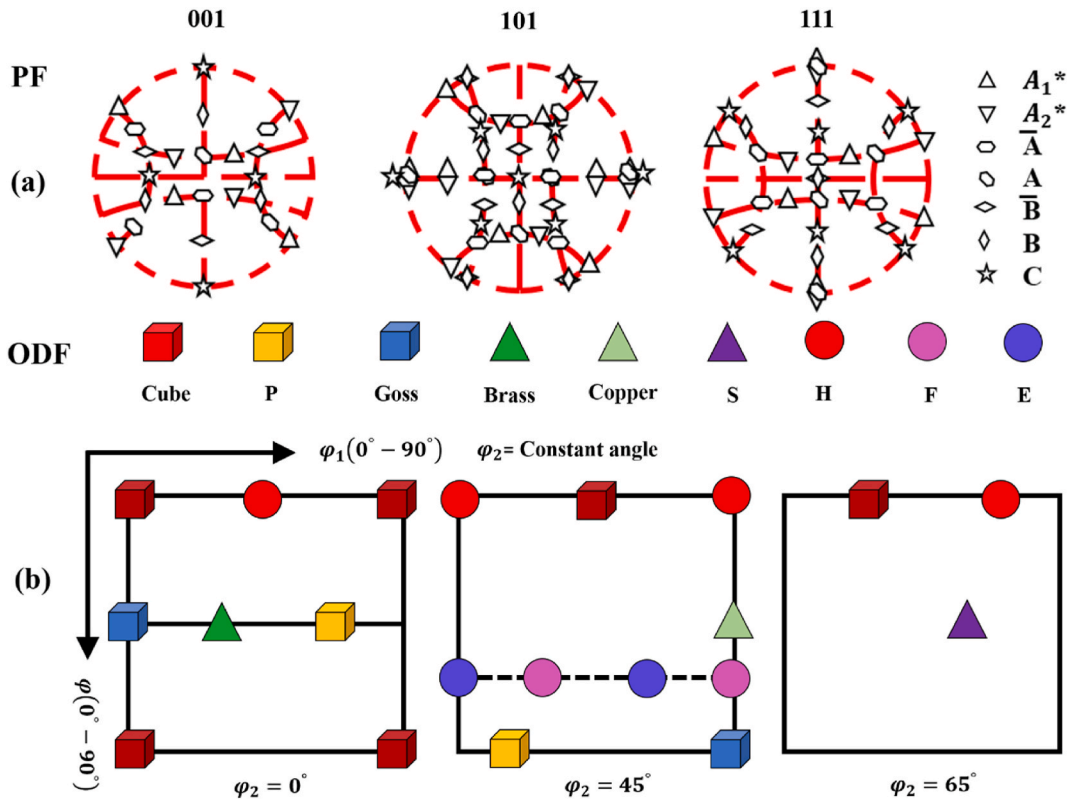


Fig. 8. (a) Shear texture elements of FCC material perfectly overlaying (001), (101), and (111) PFs, and (b) Orientation distribution function at $\varphi_2 = 0^\circ, 45^\circ,$ and $65^\circ,$ respectively [73].

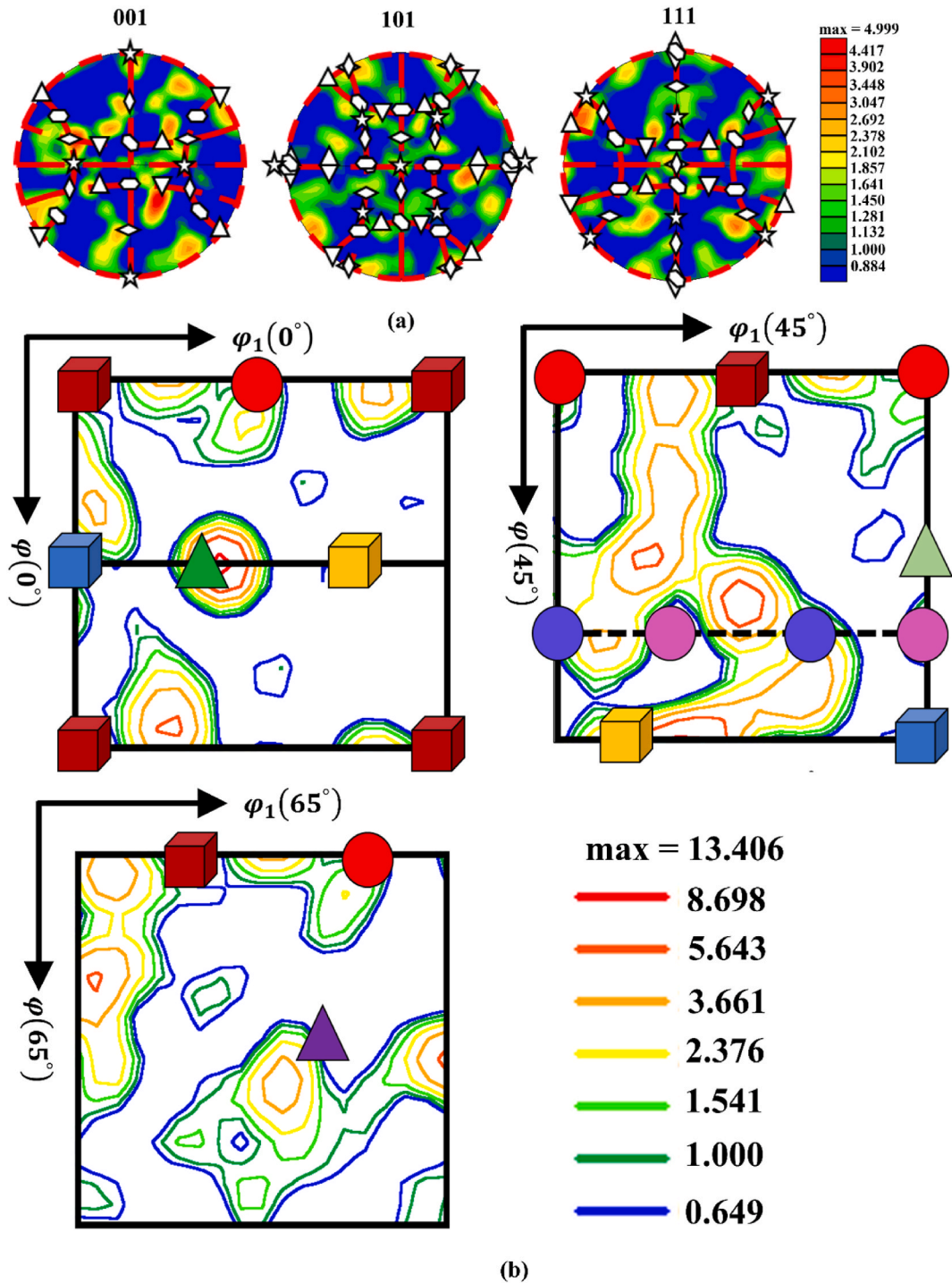


Fig. 9. Superimposed ideal shear texture component on AA7075-T6 base material: (a) PF, and (b) Orientation distribution function sections at $\phi_2 = 0^\circ, 45^\circ$, and 65° , respectively.

indicates that the weld zone of AA7075-T6, using the SQ-shaped pin profile, has undergone fully dynamic recrystallization. Additionally, the GOS map obtained from the SZ region using an SQ-shaped pin profile shows approximately 95 % of the grains have undergone recrystallization (see Fig. 7(a)). Therefore, the study proposes that complete dynamic recrystallization and significant shear deformation have occurred in the AA7075-T6 FSW joint using the SQ-shaped pin profile, as shown by the obtained texture elements in both the PFs and ODF maps.

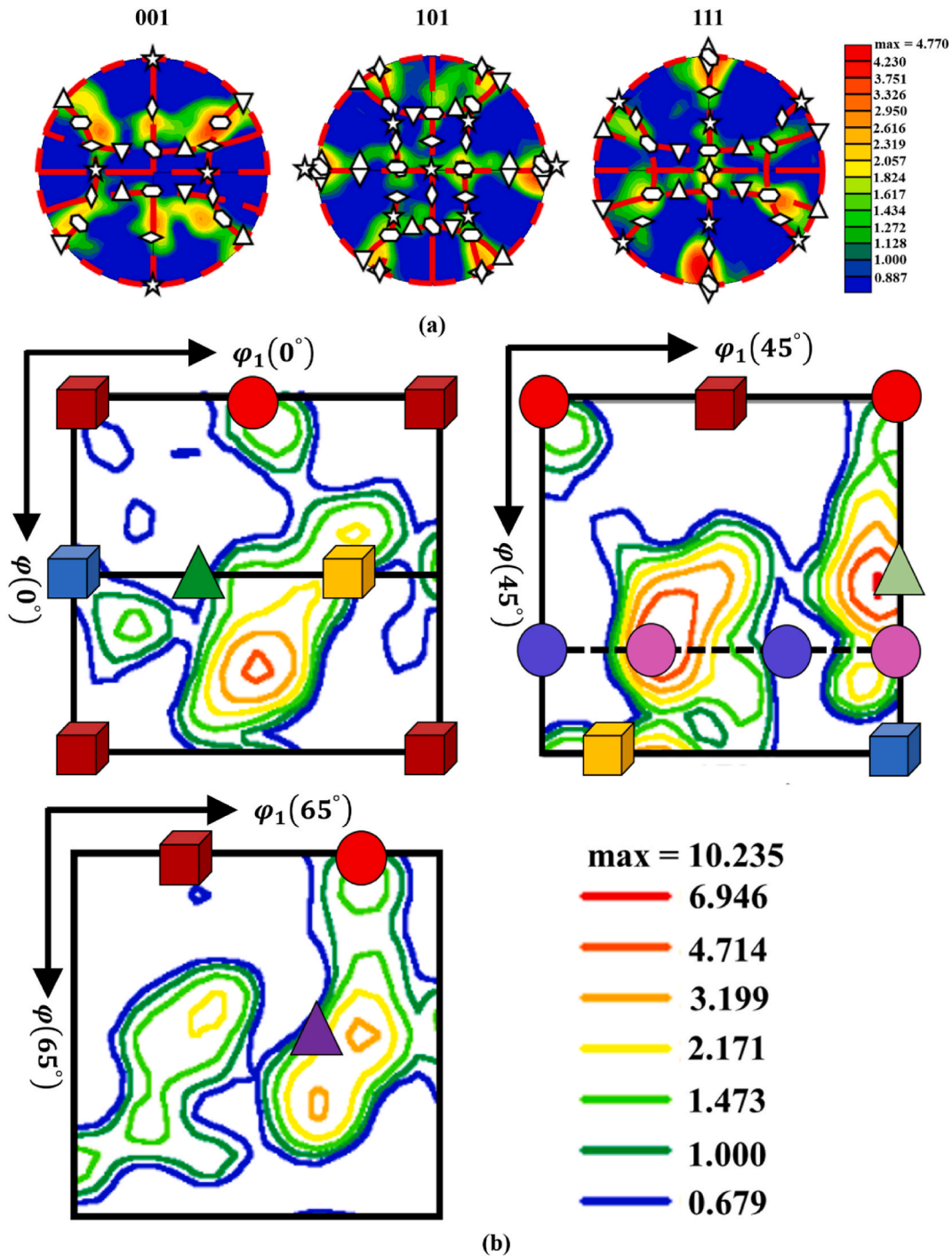


Fig. 10. Superimposed ideal shear texture component on AA7075-T6 plate weld using square-shaped pin: (a) PF, and (b) Orientation distribution function sections at $\phi_2 = 0^\circ, 45^\circ$, and 65° , respectively.

Additionally, the theoretical texture elements of AA7075-T6 are overlaid onto (001), (101), and (111) pole figures and ODF sections at $\phi_2 = 0^\circ, 45^\circ$, and 65° of the AA7075-T6 welded specimen using the HX-shaped pin profile. These PFs and ODF sections are illustrated in Fig. 11 (a and b). The analysis reveals the presence of a large number of shear elements B/ \bar{B} and C in the shear texture, along with a some A_1^* and A_2^* and A/ \bar{A} elements, indicating substantial strain within the metal. The shear texture elements intensity is stronger in the case of FSW employing the SQ-shaped pin tool (with an intensity of 4.770) compared to the HX-shaped pin tool (with an intensity of 2.868). More of the shear texture component is present in the AA7075-T6 weld SZ region using the SQ-shaped pin profile

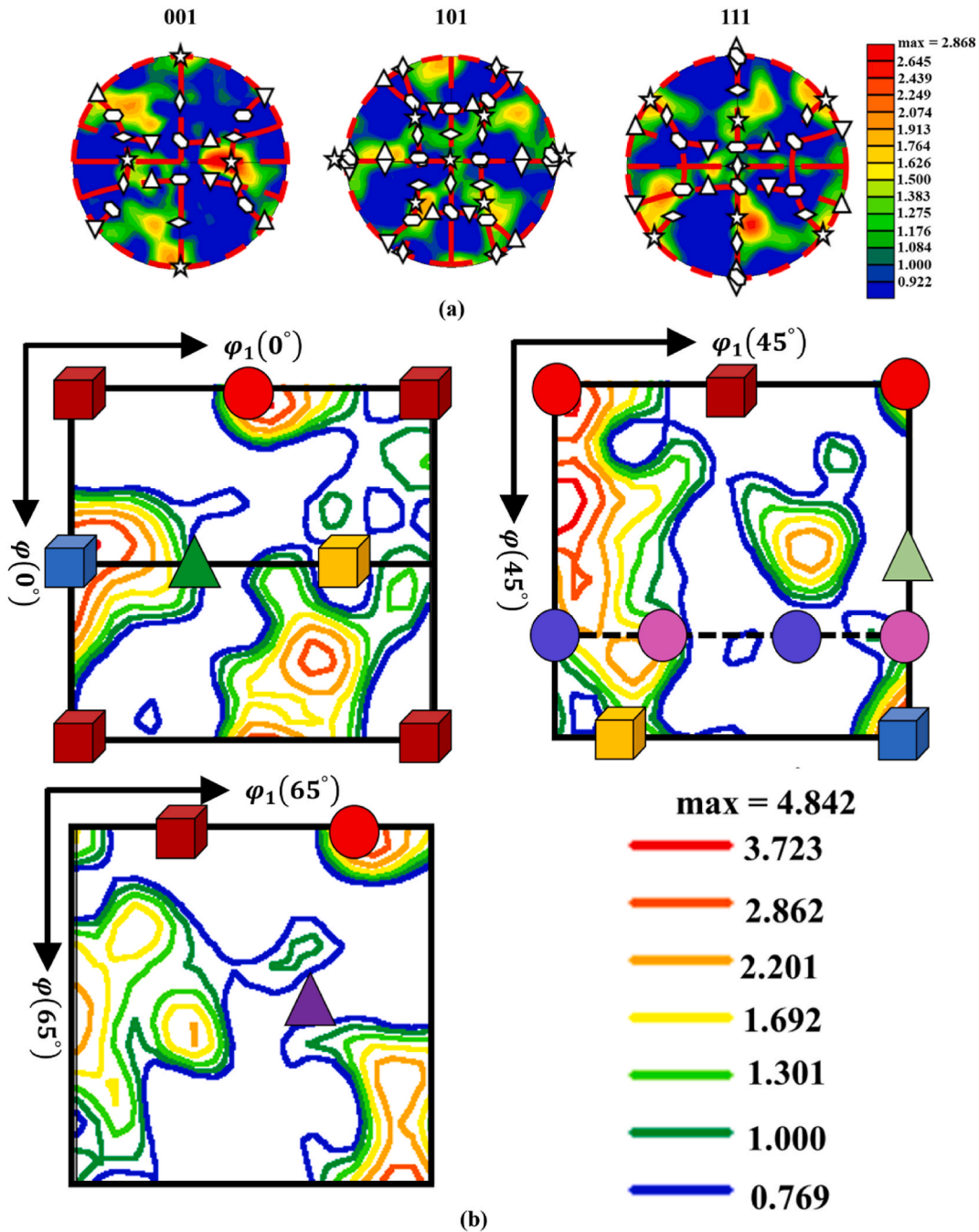


Fig. 11. Superimposed ideal shear texture component on AA7075-T6 plate weld using hexagon-shaped pin: (a) PF, and (b) Orientation distribution function sections at $\varphi_2 = 0^\circ, 45^\circ,$ and $65^\circ,$ respectively.

indicates effective material mixing during welding. Furthermore, the BM AA7075-T6 shear texture intensity is 4.999, which is nearly equivalent to the intensity of the AA7075-T6 weld joint PF when using the SQ-shaped pin, indicating considerable grain recrystallization due to substantial thermal softening of the material during welding.

Moreover, the ODF plot of the AA7075-T6 weld zone using the SQ-shaped pin profile exhibits a maximum intensity value of 10.235 (see Fig. 10(b)), significantly surpassing the ODF intensity obtained from the HX-shaped pin weld joint (4.842). Furthermore, the ODF maps (see Fig. 11(b)) for $\varphi_2 = 0^\circ, 45^\circ,$ and $65^\circ,$ when overlaid with theoretical texture elements, demonstrate a substantial presence of recrystallized texture components such as Goss $\{110\} \langle 001 \rangle$ and P $\{011\} \langle 112 \rangle,$ deformed texture components like Copper $\{112\} \langle 111 \rangle$ and Brass $\{011\} \langle 211 \rangle,$ and shear texture components such as rotating cube (H) $\{001\} \langle 110 \rangle$ and F $\{111\} \langle 112 \rangle,$ respectively. The presence of Brass $\{011\} \langle 211 \rangle,$ and Copper $\{112\} \langle 111 \rangle$ texture components indicate high plane strain and

deformation. A minor fraction of E {111} <110> and F {111} <112> texture elements signify the occurrence of shear deformation in the acquired ODF map. The lack of P {011} <112> texture component in the materials confirms that deformation and shear are prominent in the AA7075-T6 weld zone when using the HX-shaped pin after the FSW process.

3.3. Microhardness analysis

Fig. 12 illustrates a variation in microhardness exhibited on the surface of weld cross-section. The hardness variations for different weld zones (HAZ, TMAZ, and SZ) in the FSW joints, are shown in Fig. 12 in the middle region (schematically shown inside) of weld cross-section. It is noteworthy that the microhardness in all regions is lower than the AA7075-T6 BM due to thermal softening and re-precipitation in second phase particles in those areas. The SZ + TMAZ region exhibits improved microhardness compared to HAZ, which can be attributed to the grain refinement achieved through CDRX. Further, the tool profile in FSW can also have an effect on the microhardness enhancement of aluminium welds. The tool profile can influence the heat generation, material flow, and mechanical forces during the FSW process, which can affect the resulting microstructure and mechanical properties of the weld, including microhardness [74–76]. The design of the FSW pin, including its diameter, and shape can impact the material stirring and deformation during FSW. The microhardness (H_v) can be correlated with the grain size using the Hall-Petch relationship [77].

$$H_v = H_0 + \frac{k_H}{\sqrt{D_g}} \quad (1)$$

The hardness measurement in Equation (1) involves constants H_0 and k_H , related to the hardness measurement, and the average grain size D_g . In the cross-section surface of the AA7075-T6 weld, using an SQ-shaped pin profile, a maximum hardness of 148 HV_{0.2} is observed at the SZ + TMAZ interface region RS. Despite the improved microhardness in the SZ + TMAZ region, it remains lower than the BM AA7075-T6 hardness of 175 HV_{0.2}. This discrepancy contradicts the Hall-Petch relationship, which typically predicts higher microhardness with smaller grain sizes. The difference in microhardness may be attributed to precipitate coarsening and reprecipitation offsetting the microhardness gain from grain refinement of the welded region. Within the SZ area, the existence of precipitates leads to the immobilization of dislocations, thus aiding in the process of refining the grain microstructure by impeding the growth of grains [61,62]. The complex material flow during the FSW process, influenced by gradient in temperature, strain rate, and strain, results in high dislocation density in the SZ due to its high strain rate and temperature.

According to the Hall-Petch relation, the combined effects of smaller grain sizes, higher dislocation density, and increased strain within the SZ increase microhardness [77]. The weld SZ shows the amplified microhardness value due to the robust interfacial bonding that emerges from welding AA7075-T6 plates using SQ and HX-shaped pin profiles. The thermomechanical process of FSW re-distributes and fragments precipitates within the SZ region, transforming large and intricately shaped second-phase particles into smaller, equiaxed grains, ultimately resulting in an increase in microhardness.

For the AA7075-T6 weld joint produced with SQ and HX-shaped pin profiles, the mean microhardness within the SZ region is measured at 142 ± 4 HV_{0.2} and 138 ± 5 HV_{0.2}, respectively. The higher hardness in the SQ-shaped pin joint is attributed to uniform mixing, severe plastic deformation, and high strain rate, resulting from the high thermal softening of AA7075-T6 during welding by using the SQ-shaped pin. Additionally, there is a gradient in microhardness visible in the weld SZ area. The enhanced microhardness of the fabricated joint is attributed to the uniform mixing of AA7075-T6 material accomplished through the utilization of the SQ-shaped pin profile. Additionally, the process involves re-precipitation of second-phase particles and achieving ultrafine grain refinement, further contributing to this improvement during the FSW process.

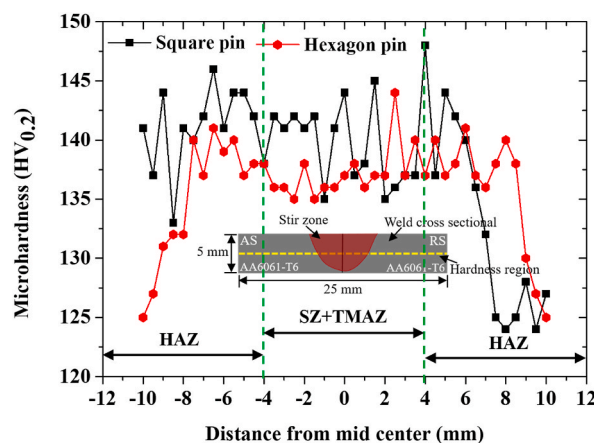


Fig. 12. Microhardness comparison plot of square and hexagon-shaped pin profiles on the middle section of the weld cross-section in the horizontal direction.

3.4. Tensile properties

Tensile tests were conducted to assess the performance of AA7075-T6 friction stir welded (FSWed) joints fabricated using two different pin profiles SQ and HX shapes. The tests measured the yield strength (YS) and ultimate tensile strength (UTS) of the joints. Fig. 13(a and b) depict the correlation between stress-strain graphs and average UTS, YS, and elongation comparison graphs for the AA7075-T6 joints produced using SQ and HX pin profiles, respectively. The joint fabricated with the SQ pin profile achieved a maximum UTS of 387 MPa and a maximum YS of 275 MPa, while the joint fabricated with the HX pin profile obtained a maximum UTS of 350 MPa and a maximum YS of 250 MPa. The lower strength observed in the joint fabricated with the HX pin profile is attributed to a defect present at the bottom of the joint in region R4, as observed in the optical microscope image (Fig. 3).

The presence of defects in the FSW joint reduces its tensile strength, resulting in weaker joint performance. Additionally, the AA7075-T6 joint fabricated with the SQ shape pin profile exhibits higher elongation (4.95 %) compared to the joint made with the HX shape pin profile (2.6 %). The improved UTS and YS of welds made using the SQ shape pin profile are attributed to various factors. These include enhanced interfacial bonding, a more homogeneous distribution of second-phase particles, re-precipitation phenomena, and grain refinement. The uniformly dispersed second-phase particles and precipitates act as sites for dislocation pileup during tensile loading, significantly enhancing the material's strength.

Furthermore, the FSW tool's stirring action breaks up larger grains, which helps the SZ region's formation of finer, more uniformly placed grains. These smaller grains contribute to enhancing mechanical properties, including heightened hardness and improved fatigue resistance [65,58,60]. Additionally, the strength of the AA7075-T6 FSW joint is greatly increased by the second-phase particles present in the SZ. As the FSW tool moves along the adjoining interface of the AA7075-T6 material, these second-phase particles disperse throughout the weld area. These compounds from the second phase contribute to refining the grain structure within the SZ area.

Further the grain refinement tends to correlate with an augmentation in tensile strength. The formation of finer grains results in a heightened density of grain boundaries, impeding dislocation movement and thereby strengthening the material's overall strength [66,61]. The development of fine equiaxed grains is a distinct result of dynamic recrystallization, a process triggered by intense plastic deformation [62]. This occurrence results in the generation of novel, smaller grains, subsequently impacting the mechanical properties of the material. Moreover, the FSW tool's rotational and translational motion brings about changes in texture within aluminium alloys. This shift in grain orientation leads to a more randomized texture, presenting potential advantages for improving mechanical properties [62,63,67].

Moreover, the AA7075-T6 joint produced using the SQ and HX shape pin profiles exerts a noteworthy influence on material flow, heat generation, and mixing within the weld zone during the FSW process. The FSW joint fabricated with the SQ shape pin profile generates more frictional heat during welding because of its larger contact area with the workpiece. This elevated frictional heating causes greater thermal softening of the material. The augmented heat input can impact the material flow and microstructure in the weld zone, thereby contributing to the enhancement of the joint's tensile strength. However, in the case of the weld zone fabricated using the HX shape pin profile, defects may arise due to insufficient material mixing. This can lead to a non-uniform distribution of alloying elements and microstructural inhomogeneity, resulting in weaker joint strength.

Additionally, as shown in Fig. 13(a), the tensile specimen image for the joint fabricated using the HX shape pin exhibits failure within the welded region (SZ), whereas the joint made with the SQ shape pin fails from the HAZ region. Overall, the use of the SQ shape pin profile can lead to more controlled and efficient welding processes, resulting in improved weld quality and enhanced mechanical properties (UTS and YS). Moreover, the elongation in SQ shape pin welded joints is higher due to factors such as more uniform material mixing, a defect-free joint, better grain refinement, and microstructural homogeneity within the weld region. The uniform mixing achieved with the SQ pin in the AA7075-T6 weld region contributes to a consistent distribution of alloying elements, which in turn enhances the overall ductility (elongation) of the joint. Overall, Table 3 provides a comparison of the mechanical properties of joints welded using SQ and HX shape tool pin profiles.

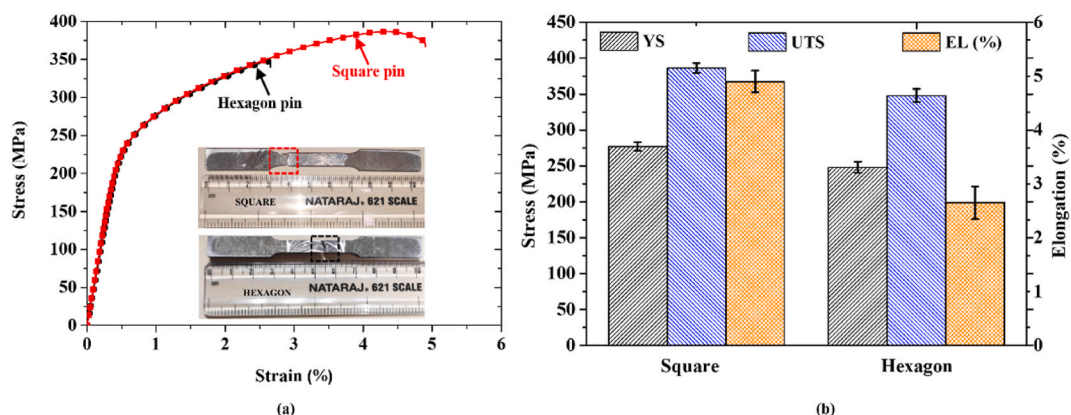


Fig. 13. Comparison plots of (a) stress-strain and (b) strength-elongation for square and hexagon-shaped pin weld specimens.

Table 3
Mechanical properties of the AA7075-T6 FSWed joint.

AA 7075-T6 FSW joint	Tensile strength	Yields strength	Elongation	Microhardness
Square pin	387 MPa	275 MPa	4.95 %	142 ± 4 HV _{0.2}
Hexagon pin	350 MPa	250 MPa	2.6 %	138 ± 5 HV _{0.2}

3.5. Strain hardening behaviour

Furthermore, a plot of true stress-strain relationship of FSWed joint made by SQ and HX shape pin profile is shown in Fig. 14(a). The true stress and true elongation of an SQ-shaped pin AA7075-T6 weld joint have a higher value than an HX-shaped pin weld joint. Also, Fig. 14(b) shows the rate of strain hardening ($\theta = \frac{d\sigma}{d\epsilon}$) graph for AA7075-T6 joint fabricated using SQ and HX shape pin profiles. The strain hardening rate of the AA7075-T6 FSWed joint was evaluated by using a Kocks–Mecking plot approach [78–80]. The strain hardening behaviour of AA7075-T6 joints is influenced by various factors, including grain refinement, dislocation density, texture modifications, microstructure, and precipitate evolution.

Typically, the strain hardening behaviour can be observed in four stages. In the initial stage (stage I) of plastic deformation, the material exhibits an intense and rapid increase in strain-hardening rate as dislocation density rises sharply due to plastic deformation. Following this initial stage, the strain-hardening rate decreases due to dislocation annihilation, and then, during stage II, it increases again as new dislocations pile up near the grain boundary. During stage III, dislocation storage is balanced by recovery and annihilation, leading to a nearly constant strain-hardening rate. In the final stage (stage IV), the strain-hardening rate experiences a rapid decline due to significant plastic deformation causing stress concentration in localized regions, leading to localized necking, final fracture, and failure [78]. The presence of stages III and IV are prominent noticeable in the FSWed samples. The joint created using the SQ-shaped pin initially demonstrates the highest strain hardening rate, attributed to its uniform material mixing and grain refinement, which create sites for dislocation accumulation. As stage III progresses, the strain hardening rate gradually diminishes due to dislocation elimination and the occurrence of dynamic recovery. Conversely, the FSWed joint formed using the HX-shaped pin profile exhibits a lower strain hardening rate in comparison to the SQ-shaped pin. To gain deeper insight into the hardening behaviour, a comparison is made regarding the AA7075-T6 joints made using the SQ and HX pin profiles in terms of their hardening capacity (H_C). According to the Hall-Petch equation [68], both the YS and the grain size have an impact on the H_C . The hardening capacity equation is [79]:

$$H_C = \frac{UTS - YS}{YS} = \frac{UTS}{YS} - 1 \quad (2)$$

The H_C values for AA7075-T6 weld joints fabricated by SQ and HX shape pin profiles are 0.407 and 0.400, respectively as calculated from Equation (2). A minor difference in H_C value is observed in both cases, indicating that the joint welded with SQ and HX shape pin profiles is stronger and harder as it is deformed.

3.6. Nanoindentation analysis

Nanoindentation experiments were conducted on the SZ, TMAZ, and HAZ regions of AA7075-T6 weld specimens to characterize their local mechanical properties. Fig. 15(a) illustrates the load-displacement curves obtained for the joints welded using the SQ shape pin profile. The average indentation depths recorded were 1064 nm, 1312 nm, 1339 nm, and 1000 nm for the SZ, TMAZ, HAZ, and base metal (AA7075), respectively. The SZ region shows a lower indentation depth, and its value is very close to BM indentation depth

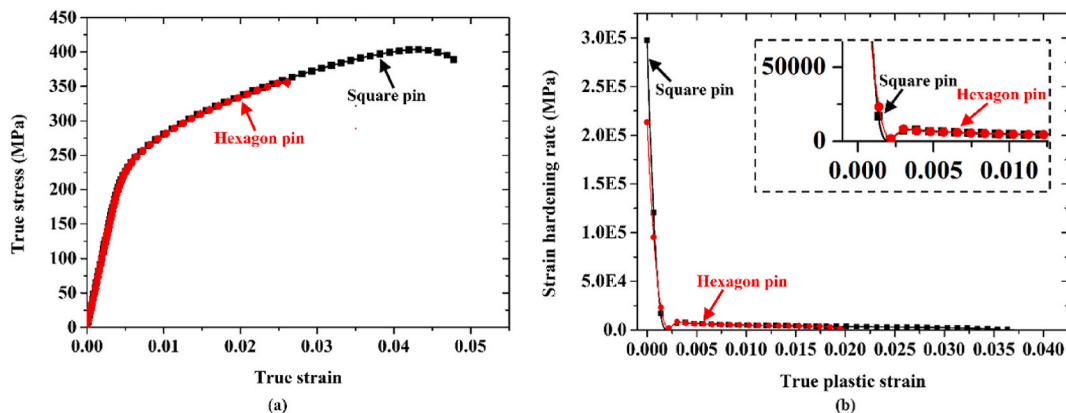


Fig. 14. (a) Plot of true stress-strain relationship, and (b) graph illustrating the rate of strain hardening, for samples subjected to welding using square and hexagon-shaped pins.

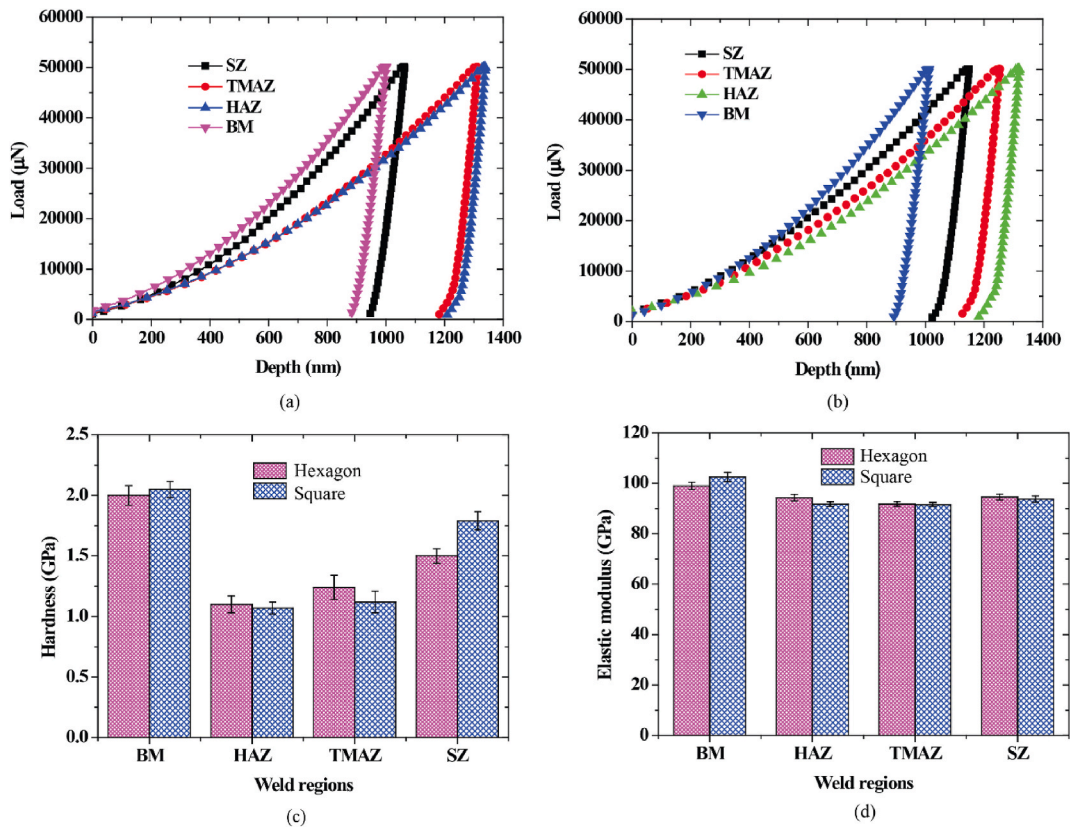


Fig. 15. (a) Nano-indentation plot of load-displacement for weld joint regions using square-shaped pin, and (b) for weld joint regions using hexagon-shaped pin. Comparison of (c) hardness and (d) elastic modulus at different weld regions for AA7075-T6 samples welded with square and hexagon pins, respectively.

compared to other regions, indicating the hardness of the SZ region after welding by using an SQ shape pin is close to BM AA7075-T6 hardness. Also, in the microhardness plot, it is clear that joints fabricated using the SQ shape pin have a higher hardness in the SZ region (see Fig. 12). Further, Fig. 15(b) shows the load-displacement curve in different weld zones of an AA7075-T6 weld joint fabricated by an HX shape pin profile. In this case, the indentation depths are 1149 nm, 1254 nm, 1320 nm, and 1012 nm for SZ, TMAZ, HAZ, and BM 7075-T6, respectively. Here also, the indentation depth in SZ is close to the BM indentation depth, which indicates the high hardness within the SZ area, as clarified from the microhardness plot of HX shape pin weld region.

Furthermore, Fig. 15(c and d) depict the average hardness and elastic modulus values for the SZ, TMAZ, HAZ, and base metal (AA7075-T6) of weld specimens fabricated using SQ and HX pin profiles. The SZ region of the FSW joint produced by the SQ shape pin exhibits the highest hardness and elastic modulus, in accordance with the microhardness results (as shown in Fig. 12). On the other hand, the HX shape pin profile weld specimen shows relatively lower hardness and elastic modulus in the SZ region. The SZ region displays a higher standard deviation in hardness values, which can be attributed to variations in microstructure and strain gradient (as depicted in Figs. 5 and 6). These combined effects of inhomogeneous microstructure and varying strain result in differences in the mechanical properties across different locations within the SZ region. Specifically, the hardness of the material is influenced. Further, regions with finer grains and lower strain tend to exhibit higher hardness, while areas with coarser grains and higher strain typically have lower hardness. The microstructure of a material plays a pivotal role in determining its mechanical properties, particularly at the nanoscale. The material's nanomechanical behavior can be significantly influenced by different aspects of its microstructure, including grain size, precipitate evolution, dislocations, and grain orientation.

Moreover, the theoretical Nix-Gao model is frequently used to evaluate nanoindentation data and develop an understanding of the mechanical properties of materials at the nanoscale. In nanoindentation, a small and pointed Berkovich indenter, having a pyramid-shaped diamond tip, is pressed into the material's surface, resulting in the formation of a hemispherical plastic deformation zone. The following equation is used to estimate the diameter of the plastic deformation zone [81]:

$$2r = 2a \approx 8.7h \quad (3)$$

Equation (3) incorporates the average indentation depth from different locations in the AA7075-T6 FSWed joint, welded using SQ and HX shape pin profiles, to calculate the diameter of the plastic deformation zone ($2r$). The values of 'a' and 'h' represent the indentation radius and maximum indentation depth, respectively. The dimensions of the plastically deformed zone are 9.99 μm, 10.91

μm , and $11.48 \mu\text{m}$ in the SZ, TMAZ, and HAZ regions of the HX shape weld specimen, respectively. Conversely, the SQ shape pin weld specimen exhibits plastic deformation zones with dimensions of $9.25 \mu\text{m}$, $11.41 \mu\text{m}$, and $11.64 \mu\text{m}$, respectively. Based on these findings, the HAZ region demonstrates a higher level of plastic deformation compared to the SZ. Fig. 7 reveals that the majority of grains recrystallize in the SZ zone, whereas as we move towards the TMAZ and HAZ regions, the grains undergo plastic deformation. This again confirm weld made by SQ having high fraction of recrystallized grain compared to HX pin profile, similar to results obtained GOS map of weld SZ region (see Fig. 7). Furthermore, the diameter of the plastic deformation zone ($2r$) is smaller in the SZ region of welds created using the SQ shaped pin profile in comparison to welds made with the HX shaped pin profile. This finding supports the results obtained from welds made with the square pin profile have more recrystallized grains compared to those produced with the hexagon pin profile. This correlation aligns with the outcomes derived from the GOS map of the weld SZ area (see Fig. 7). Overall, the grain boundary remains a crucial part of the plastic deformation zone and significantly influences the estimation of nanohardness within the SZ.

3.7. Fractographic analysis

Following the tensile test, Fig. 16(a and b) display images of the fracture surfaces from the tensile failure of the AA7075-T6 weld specimens produced using the SQ and HX pin profiles, respectively. The FESEM images provide insights into the failure modes and characteristics of the welded joints after uniaxial tensile testing. Fig. 16(a) shows the fractographs of the joint welded with the SQ-shaped tool pin, showing numerous fine equiaxed dimples throughout the fracture surface. Further, a higher density of dimples on the fracture surface of an FSW joint is correlated with higher strength and ductility [71]. The density of dimples on the fracture surface is directly related to the amount of energy absorbed during deformation. Higher dimple density suggests that the material absorbed more energy before fracturing, indicating higher strength and toughness [73]. It implies that the FSW joint can withstand more load and deformation before failure. Further, the presence of numerous, closely spaced dimples suggests a fine-grained microstructure, which is often associated with improved mechanical properties [75,76]. These dimples are observed on the fracture surfaces, signifying sound bonding and a ductile failure of the joint.

Fig. 16(b) illustrates the fractographs of the welded joint produced using the HX tool pin, revealing the noticeable presence of voids or tunnels on the fracture surface. Under tensile loading, cracks initiate from these areas and propagate through the firmly bonded sections between the two plates. The fracture morphology within the welded regions shows abundant micro-voids, along with dimples, and also exhibits some shear failure marks, signifying a consistent blending and bonding between the two plates within these zones. In the case of the HX tool pin, the pressure disparity between the bottom and top of the tool pin could induce the material flow to detach

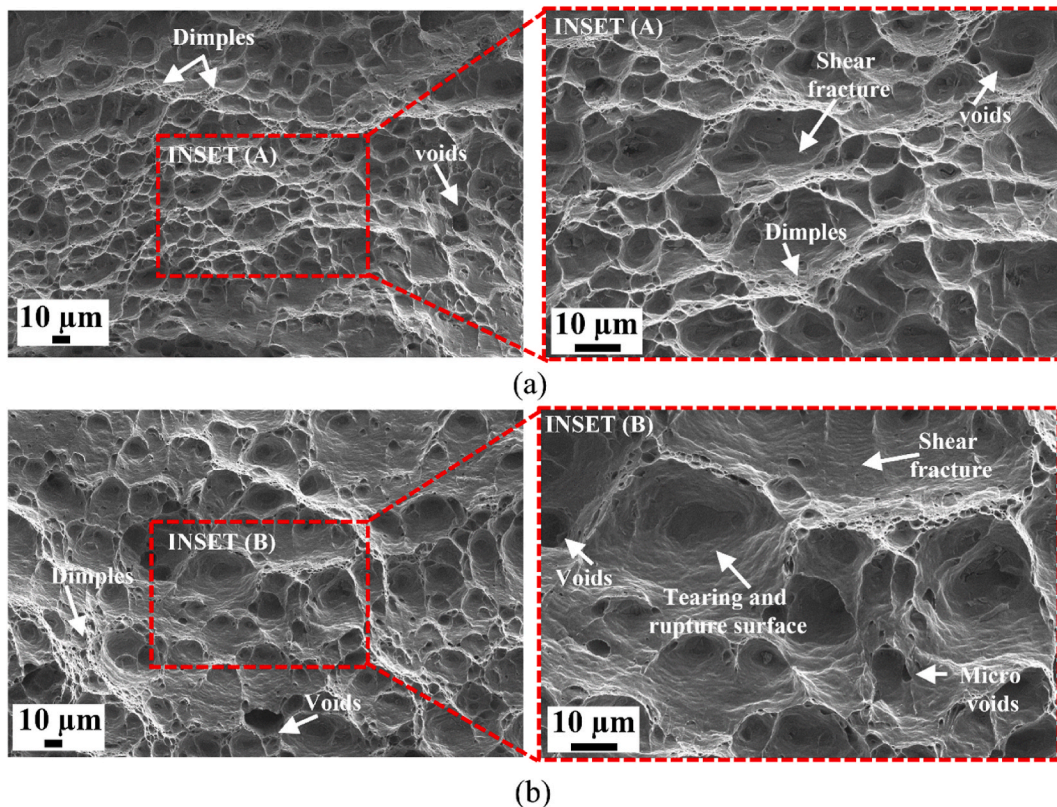


Fig. 16. Fractography images of tensile fracture surfaces for (a) square-shaped, and (b) hexagon-shaped pin profiles in FSW tool.

from the tool pin, leading to tunnel creation due to insufficient mixing of the base metal. Nevertheless, the fractographs adjacent to the tunneling region display tearing and ruptures with a certain degree of stretching, although lacking prominent dimples. This suggests brittle failure in the surrounding area of the tunnel, featuring a degree of cleavage failure pattern [23,46]. Upon comparing the fractographs of joints welded using SQ and HX tool pins, it becomes evident that ductile failure characterized by the presence of dimples is predominantly observed in well-bonded regions. Conversely, brittle-type failure involving shear, tearing, and rupture is noticeable in proximity to the tunnel or void regions. When subjected to tensile loading, the yield strength and ultimate tensile strength values rise due to the abundance of dimples and second-phase particles in the weld region. These factors collectively impede dislocation movement under tensile loading.

4. Conclusion

The present work extensively explored the microstructure, texture evolution, and mechanical properties of the friction stir welding joint of AA7075-T6 plates employing square and hexagon-shaped tool pin profiles. The following conclusions can be taken from the results:

1. The use of a square shape pin profile resulted in a defect-free joint with effective material flow and enhanced mechanical properties at the optimal process parameters of welding speed (55 mm/min) and rotational speed (850 rpm).
2. EBSD analysis revealed a significant grain refinement within the SZ of AA7075-T6 weld cross-section made using the SQ (4.43 μm) and HX (5.79 μm) shape pin profiles, compared to the base metal AA7075-T6 (32.736 μm). Notably, the weld joint fabricated using the SQ shape pin profile exhibited appreciable improvement in f_{HAGBs} and a higher fraction of recrystallized grains within the SZ compared to the joint made using the HX shape pin profile, shows the effectiveness of the CDRX mechanism during the deformation process.
3. PF analysis confirmed the presence of major shear texture components (B/ \bar{B} and C) with minor presence of A_1^*/A_2^* and A/\bar{A} , indicating the occurrence of higher strains within the SZ region. Additionally, ODF analysis revealed the existence of recrystallization texture components, such as cube {001} $\langle 101 \rangle$, P {011} $\langle 112 \rangle$, and Goss {110} $\langle 001 \rangle$, along with shear texture components, including rotating cube (H) {001} $\langle 110 \rangle$ and F {111} $\langle 112 \rangle$. The combination of these recrystallization texture components and the prevalence of main shear texture components (B/ \bar{B} and C) strongly suggests that the AA7075-T6 weld zone, utilizing the SQ-shaped pin profile, has undergone complete dynamic recrystallization.
4. The microhardness study revealed that the mean microhardness values for the AA7075-T6 weld made using SQ and HX shape tool pin profiles was $142 \pm 4 \text{ HV}_{0.2}$ and $138 \pm 5 \text{ HV}_{0.2}$, respectively. The SZ exhibited higher microhardness than the TMAZ and HAZ for both SQ and HX shape tool pin profile joints.
5. The tensile analysis revealed that the weld joint fabricated using the SQ shape pin profile exhibits superior mechanical properties compared to the weld made using the HX shape tool pin profile. The weld joint made with the SQ shape tool pin profile showed maximum UTS of 387 MPa, YS of 275 MPa, and elongation of 4.95 %. In contrast, the weld joint made with the HX shape tool pin profile exhibited lower UTS of 350 MPa, YS of 250 MPa, and elongation of 2.6 %.
6. Nanohardness analysis of the joint revealed that the weld joint made using the SQ shape tool pin profile exhibited higher hardness and modulus compared to the joint made using the HX shape pin profile.
7. Fractography analysis revealed that after tensile loading joint was welded using an SQ-shaped tool pin had numerous fine equiaxed dimples throughout the fracture surface. A higher dimple density suggests that the material absorbed more energy before fracturing, indicating higher strength and toughness.

Data availability statement

Data will be made available on request.

Additional information

No additional information is available for this paper.

CRedit authorship contribution statement

Rahul Kesharwani: Writing – original draft, Validation, Methodology, Investigation, Data curation, Conceptualization. **Kishor Kumar Jha:** Validation, Formal analysis, Data curation. **Murshid Imam:** Writing – review & editing, Supervision. **Chiranjit Sarkar:** Writing – review & editing, Supervision. **Imad Barsoum:** Writing – review & editing, Supervision.

Declaration of competing interest

The authors declare that they have no known competing financial interests or personal relationships that could have appeared to influence the work reported in this paper.

Acknowledgements

The authors are thankful to the Science and Engineering Research Board (SERB), Department of Science & Technology, Government of India, for their financial support. The authors also acknowledged FIST-DST, Government of India, for providing the Nano Indentation facility installed at IIT Patna.

References

- [1] J.V. Christy, A.H.I. Mourad, M.M. Sherif, B. Shivamurthy, Review of recent trends in friction stir welding process of aluminum alloys and aluminum metal matrix composites, *Trans. Nonferrous Metals Soc. China* 31 (2021) 3281–3309.
- [2] C. Zhang, G. Huang, Y. Cao, Y. Zhu, Q. Liu, On the microstructure and mechanical properties of similar and dissimilar AA7075 and AA2024 friction stir welding joints: effect of rotational speed, *J. Manuf. Process.* 37 (2019) 470–487.
- [3] P. Kah, R. Rajan, J. Martikainen, R. Suoranta, Investigation of weld defects in friction-stir welding and fusion welding of aluminium alloys, *Int. J. Mech. Mater. Eng.* 10 (2015) 1–10.
- [4] K.R. Ramkumar, S. Sivasankaran, F.A. Al-Mufadi, S. Siddharth, R. Raghu, Investigations on microstructure, mechanical, and tribological behaviour of AA 7075-x wt.% TiC composites for aerospace applications, *Arch. Civ. Mech. Eng.* 19 (2019) 428–438.
- [5] C. Zhang, Y. Cao, G. Huang, Q. Zeng, Y. Zhu, X. Huang, N. Li, Q. Liu, Influence of tool rotational speed on local microstructure, mechanical and corrosion behavior of dissimilar AA2024/7075 joints fabricated by friction stir welding, *J. Manuf. Process.* 49 (2020) 214–226.
- [6] Y.C. Chen, J.C. Peng, H.J. Liu, Precipitate evolution in friction stir welding of 2219-T6 aluminum alloys, *Mater. Charact.* 60 (6) (2009) 476–481.
- [7] S. Raja, M.R. Muhamad, M.F. Jamaludin, F. Yusof, A review on nanomaterials reinforcement in friction stir welding, *J. Mater. Res. Technol.* 9 (2020) 16459–16487.
- [8] A. Heidarzadeh, S. Mironov, R. Kaibyshev, G. Çam, A. Simar, A. Gerlich, F. Khodabakhshi, A. Mostafaei, D.P. Field, J.D. Robson, A. Deschamps, Friction stir welding/processing of metals and alloys: a comprehensive review on microstructural evolution, *Prog. Mater. Sci.* 117 (2021) 100752.
- [9] J. Li, M. Su, W. Qi, C. Wang, P. Zhao, F. Ni, K. Liu, Mechanical property and characterization of 7A04-T6 aluminum alloys bonded by friction stir welding, *J. Manuf. Process.* 52 (2020) 263–269.
- [10] H. Jafari, H. Mansouri, M. Honaripisheh, Investigation of residual stress distribution of dissimilar Al-7075-T6 and Al-6061-T6 in the friction stir welding process strengthened with SiO₂ nanoparticles, *J. Manuf. Process.* 43 (2019) 145–153.
- [11] R. Kesharwani, K.K. Jha, M.A.A. Anshari, M. Imam, C. Sarkar, Comparison of microstructure, texture, and mechanical properties of the SQ and thread pin profile FSW joint of AA6061-T6 with Al₂O₃ particle reinforcement, *Mater. Today Commun.* 33 (2022) 104785.
- [12] R. Kesharwani, K.K. Jha, C. Sarkar, M. Imam, Numerical and experimental analysis on friction stir welding of the dissimilar materials 6061-T6 AA and pure copper, *Mater. Today Proc.* 65 (2022) 3132–3142.
- [13] M.A. Wahid, N. Sharma, R. Shandley, Friction stir welding process effects on human health and mechanical properties, *Int. J. Manag. Sci.* 1 (2020) 42–52.
- [14] X. Meng, Y. Huang, J. Cao, J. Shen, J.F. dos Santos, Recent progress on control strategies for inherent issues in friction stir welding, *Prog. Mater. Sci.* 115 (2021) 100706.
- [15] A.K. Kadian, P. Biswas, The study of material flow behaviour in dissimilar material FSW of AA6061 and Cu-B370 alloys plates, *J. Manuf. Process.* 34 (2018) 96–105.
- [16] V.P. Singh, S.K. Patel, A. Ranjan, B. Kuriachen, Recent research progress in solid state friction-stir welding of aluminium–magnesium alloys: a critical review, *J. Mater. Res. Technol.* 9 (3) (2020) 6217–6256.
- [17] M.A.A. Anshari, R. Mishra, M. M. Imam, D. Pandit, K.K. Jha, R. Kesharwani, M. Kar, V. Chinthapenta, Comparison of the microstructures and mechanical properties in the Overlapping region of low Carbon steel additive bead fabricated by WAAM and FSP, *Metall. Mater. Trans. A* 54 (2023) 869–895.
- [18] A. Chaudhary, R. Mishra, M.A.A. Anshari, M. Imam, V. Chintapenta, Experimental and numerical investigation of laser-FSW hybrid welding technique for high strength materials, *Mater. Today Proc.* 65 (2022) 3437–3448.
- [19] F. Ye, H. Fujii, T. Tsumura, K. Nakata, Friction stir welding of Inconel alloy 600, *J. Mater. Sci.* 41 (2006) 5376–5379.
- [20] K.K. Jha, M.A.A. Ansari, Investigation on single/double pass friction stir processing techniques of nickel 200 alloy, *Mater. Today Proc.* 56 (2022) 722–725.
- [21] A. Kar, D. Yadav, S. Suwas, S.V. Kailas, Role of plastic deformation mechanisms during the microstructural evolution and intermetallics formation in dissimilar friction stir weld, *Mater. Charact.* 164 (2020) 110371.
- [22] K. Inada, H. Fujii, Y.S. Ji, Y.F. Sun, Y. Morisada, Effect of gap on FSW joint formation and development of friction powder processing, *Sci. Technol. Weld. Join.* 14 (2010) 131–136.
- [23] R. Kesharwani, K.K. Jha, M. Imam, C. Sarkar, The optimization of the groove depth height in friction stir welding of AA 6061-T6 with Al₂O₃ powder particle reinforcement, *J. Mater. Res.* 37 (2022) 3743–3760.
- [24] K.K. Jha, R. Kesharwani, M. Imam, Microstructure and mechanical properties correlation of FSAM employed AA5083/AA7075 Joints, *Trans. Indian Inst. Met.* 76 (2023) 323–333.
- [25] M. Rahmi, M. Abbasi, Friction stir vibration welding process: modified version of friction stir welding process, *Int. J. Adv. Manuf. Technol.* 90 (2017) 141–151.
- [26] S. Fouladi, M. Abbasi, The effect of friction stir vibration welding process on characteristics of SiO₂ incorporated joint, *J. Mater. Process. Technol.* 243 (2017) 23–30.
- [27] Y. Ni, L. Fu, Z. Shen, X.C. Liu, Role of tool design on thermal cycling and mechanical properties of a high-speed micro friction stir welded 7075-T6 aluminum alloy, *J. Manuf. Process.* 48 (2019) 145–153.
- [28] M. Mirzaei, P. Asadi, A. Fazli, Effect of tool pin profile on material flow in double shoulder friction stir welding of AZ91 magnesium alloy, *Int. J. Mech. Sci.* 183 (2020) 105775.
- [29] R. Rai, A. De, H.K.D.H. Bhadeshia, T. DebRoy, Friction stir welding tools, *Sci. Technol. Weld. Join.* 16 (2011) 325–342.
- [30] A.S. Sundar, A. Kar, K.K. Mugada, A. Kumar, Enhancement of microstructure, micro-texture, and mechanical properties of Al6061 friction stir welds using the developed static shoulder welding tool, *Mater. Charact.* 203 (2023) 113148.
- [31] K. Ramanjaneyulu, G. Madhusudhan Reddy, A. Venugopal Rao, Role of tool shoulder diameter in friction stir welding: an analysis of the temperature and plastic deformation of AA 2014 aluminum alloy, *Trans. Indian Inst. Met.* 67 (2014) 769–780.
- [32] J. Schneider, S. Brooke, A.C. Nunes, Material flow modification in a FSW through introduction of flats, *Metall. Mater. Trans. B* 47 (2016) 720–730.
- [33] V.V. Patel, V. Badheka, A. Kumar, Effect of polygonal pin profiles on friction stir processed superplasticity of AA7075 alloy, *J. Mater. Process. Technol.* 240 (2017) 68–76.
- [34] H. Su, C.S. Wu, M. Bachmann, M. Rethmeier, Numerical modeling for the effect of pin profiles on thermal and material flow characteristics in friction stir welding, *Mater. Des.* 77 (2015) 114–125.
- [35] K. Elangovan, V. Balasubramanian, Influences of tool pin profile and welding speed on the formation of friction stir processing zone in AA2219 aluminium alloy, *J. Mater. Process. Technol.* 200 (2008) 163–175.
- [36] S.M. Bayazid, H. Farhangi, A. Ghahramani, Effect of pin profile on defects of friction stir welded 7075 aluminum alloy, *Procedia Mater. Sci.* 11 (2015) 12–16.
- [37] K. Elangovan, V. Balasubramanian, Influences of tool pin profile and tool shoulder diameter on the formation of friction stir processing zone in AA6061 aluminium alloy, *Mater. Des.* 29 (2008) 362–373.
- [38] M. Ilangovan, S.R. Boopathy, V. Balasubramanian, Effect of tool pin profile on microstructure and tensile properties of friction stir welded dissimilar AA 6061-AA 5086 aluminium alloy joints, *Def. Technol.* 11 (2015) 174–184.

- [39] M.M. Khalilabad, Y. Zedan, D. Texier, M. Jahazi, P. Bocher, Effect of tool geometry and welding speed on mechanical properties of dissimilar AA2198–AA2024 FSWed joint, *J. Manuf. Process.* 34 (2018) 86–95.
- [40] Z. Li, Y. Yue, S. Ji, C. Peng, L. Wang, Optimal design of thread geometry and its performance in friction stir spot welding, *Mater. Des.* 94 (2016) 368–376.
- [41] P. Mastanaiah, A. Sharma, G.M. Reddy, Role of hybrid tool pin profile on enhancing welding speed and mechanical properties of AA2219-T6 friction stir welds, *J. Mater. Process. Technol.* 257 (2018) 257–269.
- [42] H. Zhang, M. Wang, X. Zhang, G. Yang, Microstructural characteristics and mechanical properties of bobbin tool friction stir welded 2A14-T6 aluminum alloy, *Mater. Des.* 65 (2015) 559–566.
- [43] M.K. Sued, D.J. Pons, Dynamic interaction between machine, tool, and substrate in bobbin friction stir welding, *Int. J. Manuf. Eng.* 2016 (2016) 1–14.
- [44] K.K. Jha, R. Kesharwani, M. Imam, Microstructural and micro-hardness study on the fabricated Al 5083-O/6061-T6/7075-T6 gradient composite component via a novel route of friction stir additive manufacturing, *Mater. Today Proc.* 56 (2022) 819–825.
- [45] R. Kesharwani, K.K. Jha, C. Sarkar, M. Imam, Numerical and experimental studies on friction stir welding of 6061-T6 AA with Al₂O₃ powder particle reinforcement, *Mater. Today Proc.* 56 (2022) 826–833.
- [46] R. Kesharwani, K.K. Jha, M. Imam, C. Sarkar, The optimization of gap width size during friction stir welding of AA 6061-T6 with Al₂O₃ particle reinforcement, *J. Mater. Eng. Perform.* 32 (2022) 6008–6027.
- [47] N.D. Ghate, A. Sood, A. Srivastava, A. Shrivastava, Ductile fracture based joint formation mechanism during friction stir welding, *Int. J. Mech. Sci.* 168 (2020) 105293.
- [48] H. He, Z. Liu, Y. Zhu, J. Chu, S. Li, S. Pei, C. Zhang, A. Fu, W. Zhao, Mechanism of pin thread and flat features affecting material thermal flow behaviours and mixing in Al-Cu dissimilar friction stir welding, *Int. J. Mech. Sci.* 260 (2023) 108615.
- [49] R. Kesharwani, M. Imam, C. Sarkar, Effect of flat probe on local heat generation and microstructural evolution in friction stir welding of 6061-T6 aluminium alloy, *Trans. Indian Inst. Met.* 74 (2021) 3185–3203.
- [50] C.G. Rhodes, M.W. Mahoney, W.H. Bingel, R.A. Spurling, C.C. Bampton, Effects of friction stir welding on microstructure of 7075 aluminum, *Scr. Mater.* 36 (1997) 69–75.
- [51] M.W. Mahoney, C.G. Rhodes, J.G. Flintoff, W.H. Bingel, R.A. Spurling, Properties of friction-stir-welded 7075 T651 aluminum, *Metall. Mater. Trans. A* 29 (1998) 1955–1964.
- [52] P. Prakash, S.K. Jha, S.P. Lal, Numerical investigation of stirred zone shape and its effect on mechanical properties in friction stir welding process, *Weld. World* 63 (2019) 1531–1546.
- [53] R. Raja, A. Parthiban, S. Nandha Gopan, D. Degefa, Investigate the process parameter on the friction stir welding of dissimilar aluminium alloys, *Adv. Mater. Sci. Eng.* (2022) 1–8.
- [54] M.M. El-Sayed, A.Y. Shash, M. Abd-Rabou, M.G. ElSherbiny, Welding and processing of metallic materials by using friction stir technique: a review, *J. Adv. Join. Process.* 3 (2021) 100059.
- [55] D.G. Andrade, C. Leitão, N. Dialami, M. Chiumenti, D.M. Rodrigues, Modelling torque and temperature in friction stir welding of aluminium alloys, *Int. J. Mech. Sci.* 182 (2020) 105725.
- [56] M.P. Iqbal, A. Tripathi, R. Jain, R.P. Mahto, S.K. Pal, P. Mandal, Numerical modelling of microstructure in friction stir welding of aluminium alloys, *Int. J. Mech. Sci.* 185 (2020) 105882.
- [57] D.G. Andrade, C. Leitão, N. Dialami, M. Chiumenti, D.M. Rodrigues, Analysis of contact conditions and its influence on strain rate and temperature in friction stir welding, *Int. J. Mech. Sci.* 191 (2021) 106095.
- [58] V. Chitturi, S.R. Pedapati, M. Awang, Challenges in dissimilar friction stir welding of aluminum 5052 and 304 stainless steel alloys, *Materwiss Werkstsch* 51 (2020) 811–816.
- [59] V.P. Singh, S.K. Patel, A. Ranjan, B. Kuriachen, Recent research progress in solid state friction-stir welding of aluminium–magnesium alloys: a critical review, *J. Mater. Res. Technol.* 9 (2020) 6217–6256.
- [60] I. Galvão, J.C. Oliveira, A. Loureiro, D.M. Rodrigues, Formation and distribution of brittle structures in friction stir welding of aluminium and copper: influence of shoulder geometry, *Intermetallics* 22 (2012) 122–128.
- [61] V.K.S. Jain, K.U. Yazar, S. Muthukumar, Development and characterization of Al5083-CNTs/SiC composites via friction stir processing, *J. Alloys Compd.* 798 (2019) 82–92.
- [62] T.R. McNelley, S. Swaminathan, J.Q. Su, Recrystallization mechanisms during friction stir welding/processing of aluminum alloys, *Scr. Mater.* 58 (2008) 349–354.
- [63] G. Liu, L.E. Murr, C.S. Niou, J.C. McClure, F.R. Vega, Microstructural aspects of the friction-stir welding of 6061-T6 aluminum, *Scr. Mater.* 37 (3) (1997) 355–361.
- [64] B. Heinz, B. Skrotzki, Characterization of a friction-stir-welded aluminum alloy 6013, *Metall. Mater. Trans. B* 33 (2002) 489–498.
- [65] K.V. Jata, K.K. Sankaran, J.J. Ruschau, Friction-stir welding effects on microstructure and fatigue of aluminum alloy 7050-T7451, *Metall. Mater. Trans. A* 31 (2000) 2181–2192.
- [66] Y.S. Sato, H. Kokawa, M. Enomoto, S. Jogan, Microstructural evolution of 6063 aluminum during friction-stir welding, *Metall. Mater. Trans. A* 30 (1999) 2429–2437.
- [67] M.M. Moradi, H.J. Aval, R. Jamaati, S. Amirkhanlou, S. Ji, Effect of SiC nanoparticles on the microstructure and texture of friction stir welded AA2024/AA6061, *Mater. Charact.* 152 (2019) 169–179.
- [68] J.Q. Su, T.W. Nelson, C.J. Sterling, Microstructure evolution during FSW/FSP of high strength aluminum alloys, *Mater. Sci. Eng. A* 405 (2005) 277–286.
- [69] B. Bagheri, M. Abbasi, Development of AZ91/SiC surface composite by FSP: effect of vibration and process parameters on microstructure and mechanical characteristics, *Adv. Manuf.* 8 (2020) 82–96.
- [70] O.S. Salih, H. Ou, W. Sun, D.G. McCartney, A review of friction stir welding of aluminium matrix composites, *Mater. Des.* 86 (2015) 61–71.
- [71] K.K. Jha, R. Kesharwani, M. Imam, Microstructure, texture, and mechanical properties correlation of AA5083/AA6061/SiC composite fabricated by FSAM process, *Mater. Chem. Phys.* 296 (2023) 127210.
- [72] H.W. Yang, I.P. Widiyantara, Y.G. Ko, Effect of deformation path on texture and tension properties of submicrocrystalline Al-Mg-Si alloy fabricated by differential speed rolling, *Mater. Lett.* 213 (2018) 54–57.
- [73] R. Kesharwani, K.K. Jha, M. Imam, C. Sarkar, I. Barsoum, Comparison of microstructural, texture and mechanical properties of SiC and Zn particle reinforced FSW 6061-T6 aluminium alloy, *J. Mater. Res. Technol.* 26 (2023) 3301–3321.
- [74] A. Garg, A. Bhattacharya, Effect of tool size on AA6061-T6 double-sided friction stir welds, *Mater. Des. Process. Commun.* 3 (5) (2021) e259.
- [75] A. Garg, M. Raturi, A. Bhattacharya, Strength, failure and microstructure development for friction stir welded AA6061-T6 joints with different tool pin profiles, *CIRP J. Manuf. Sci. Technol.* 29 (2020) 99–114.
- [76] K. Elangovan, V. Balasubramanian, M. Valliappan, Influences of tool pin profile and axial force on the formation of friction stir processing zone in AA6061 aluminium alloy, *Int. J. Adv. Manuf. Technol.* 38 (2008) 285–295.
- [77] N. Hansen, Hall–Petch relation and boundary strengthening, *Scr. Mater.* 51 (2004) 801–806.
- [78] U.F. Kocks, H. Mecking, Physics and phenomenology of strain hardening: the FCC case, *Prog. Mater. Sci.* 48 (2003) 171–273.
- [79] N. Afrin, D.L. Chen, X. Cao, M. Jahazi, Strain hardening behavior of a friction stir welded magnesium alloy, *Scr. Mater.* 57 (2007) 1004–1007.
- [80] W.F. Xu, J.H. Liu, D.L. Chen, G.H. Luan, J.S. Yao, Improvements of strength and ductility in aluminum alloy joints via rapid cooling during friction stir welding, *Mater. Sci. Eng. A* 548 (2012) 89–98.
- [81] W.D. Nix, H. Gao, Indentation size effects in crystalline materials: a law for strain gradient plasticity, *J. Mech. Phys. Solids* 46 (1998) 411–425.